Early deglacial CO2 release from the Sub-Antarctic Atlantic and Pacific oceans

Shuttleworth R. [1], Bostock H.C. [2, 3], Chalk T.B. [1, 4], Calvo E. [5, 6], Jaccard S.L., Pelejero C. [4, 7], Martínez-García A. [8], Foster G.L. [1, *]

[1] School of Ocean and Earth Science, University of Southampton, National Oceanography Centre Southampton, Waterfront Campus, European Way, Southampton, SO14 3ZH, United Kingdom
[2] School of Earth and Environmental Science, University of Queensland, Brisbane, Queensland, Australia
[3] National Institute of Water and Atmosphere, Wellington, New Zealand
[4] Institut de Ciències del Mar, ICM-CSIC, Barcelona, Catalonia, Spain
[5] Institute of Geological Sciences and Oeschger Center for Climate Change Research, University of Bern, 3012 Bern, Switzerland
[6] Institute of Earth Sciences, University of Lausanne, 1015 Lausanne, Switzerland
[7] Institució Catalana de Recerca i Estudis Avançats (ICREA), Barcelona, Catalonia, Spain
[8] Max-Planck-Institut für Chemie, (Otto-Hahn-Institut), Hahn-Meitner-Weg 1, 55128 Mainz, Germany

* Corresponding author : G. L. Foster, email address : g.foster@soton.ac.uk

Abstract :

Over the last deglaciation there were two transient intervals of pronounced atmospheric CO2 rise; Heinrich Stadial 1 (17.5-15 kyr) and the Younger Dryas (12.9-11.5 kyr). Leading hypotheses accounting for the increased accumulation of CO2 in the atmosphere at these times invoke deep ocean carbon being released from the Southern Ocean and an associated decline in the global efficiency of the biological carbon pump. Here we present new deglacial surface seawater pH and CO2sw records from the Sub-Antarctic regions of the Atlantic and Pacific oceans using boron isotopes measured on the planktic foraminifera Globigerina bulloides. These new data support the hypothesis that upwelling of carbon-rich water in the Sub-Antarctic occurred during Heinrich Stadial 1, and contributed to the initial increase in atmospheric CO2. The increase in CO2sw is coeval with a decline in biological productivity at both the Sub-Antarctic Atlantic and Pacific sites. However, there is no evidence for a significant outgassing of deep ocean carbon from the Sub-Antarctic during the rest of the deglacial, including the second period of atmospheric CO2 rise coeval with the Younger Dryas. This suggests that the second rapid increase in atmospheric CO2 is driven by processes operating elsewhere in the Southern Ocean, or another region.

Highlights

► Sub-Antarctic CO_2 release contributed to early deglacial atmospheric CO_2 rise. ► No evidence for enhanced CO_2 flux from the Sub-Antarctic during the Younger Dryas. ► Large heterogeneity of CO_2 flux from the Southern Ocean over the last 20 kyr.

Keywords : deglaciation, Heinrich Stadial 1, CO2 flux, boron isotopes, Southern Ocean, Sub-Antarctic

1. Introduction

The oceans represent the largest carbon reservoir in the atmosphere-biosphere-ocean system, with the Southern Ocean being the primary region for dynamic exchange between the ocean subsurface and the atmosphere. This region therefore exerts a critical control on atmospheric CO_2 levels on various timescales (Sigman et al., 2010). However, the underlying mechanism(s) that drove the rapid CO_2 rise during the most recent deglaciation is still a topic of debate (Galbraith and Skinner, 2020). During the last deglacial, atmospheric CO_2 increased from a stable last glacial maximum value of 190 parts per million (ppm) to pre-industrial levels of 280 ppm. This occurred over two broad, millennial scale, intervals centered around Heinrich-Stadial 1 (HS1, 17.5-15 kyr), and the Younger Dryas (YD, 12.9-11.5 kyr), punctuated by a further centennial increase at 13.8 ka (Bereiter et al., 2015; Fig. 1). This study focusses on the millennial scale episodes of atmospheric CO_2 rise. Several indirect marine proxy records from the Southern Ocean and Antarctic ice cores indicate that the rise in atmospheric CO_2 during both HS1 and the YD may be the result of enhanced upwelling of CO_2-rich subsurface waters in the Antarctic Zone (AZ) (Anderson et al., 2009, Gottschalk et al., 2016, Jaccard et al., 2016, Rae et al., 2018) and/or a decline in biological productivity in the Sub-Antarctic Zone (SAZ) of the Southern Ocean (Lamy et al., 2014, Martínez-García et al., 2014, Jaccard et al., 2016, Thöle et al., 2019).

Recent work, using the carbon isotopic signature of atmospheric CO_2 trapped in Antarctic ice cores ($\delta^{13}C_{atm}$), attempted to distinguish between different sources of carbon during the rapid rises in CO_{2atm} across the last deglaciation ((Schmitt et al., 2012, Bauska et al., 2016); Fig. 1). The initial negative $\delta^{13}C_{atm}$ excursion of -0.3 ‰ during HS1 is proposed to be either the result of enhanced Southern Ocean upwelling of ^{12}C-enriched deep water and/or a decline in the ocean biological carbon pump (Schmitt et al., 2012, Bauska et al., 2016; Fig. 1). The hypothesis of enhanced Southern Ocean overturning during HS1 is supported by a concurrent decline in $\delta^{13}C$ in the surface ocean recorded by planktic foraminifera (Ninnemann and Charles, 1997, Spero and Lea, 2002, Ziegler et al.,

68   2013), an increase in ventilation ages, reducing the radiocarbon depletion of upper circumpolar deep

69   water (Skinner et al., 2010, Burke and Robinson, 2012, Gottschalk et al., 2016), an increase in the

70   deep Southern Ocean water oxygenation (Jaccard et al., 2016, Gottschalk et al., 2016), an increase in

71   opal flux associated with upwelling in the AZ (Anderson et al., 2009; Fig. 1), and an increase in the

72   supply of deep ocean-sourced nitrate to the AZ surface (Studer et al., 2015, Wang et al., 2017). There

73   is also strong evidence for a reduction in the biological carbon pump at HS1 based on productivity

74   and nutrient proxies in Sub-Antarctic Atlantic sediment cores, likely driven by a reduction in the Fe-

75   fertilisation from aeolian dust (Jaccard et al., 2013, Anderson et al., 2014, Martínez-García et al.,

76   2014; Fig. 1). Evidence from the Sub-Antarctic Pacific suggests smaller changes in export production

77   between the Last Glacial Maximum (LGM) and the Holocene (Chase et al., 2003, Bradtmiller et al.,

78   2009, Lamy et al., 2014). The role of this region in deglacial CO_2 rise therefore remains uncertain.

79   Following HS1, during the Bølling-Allerød/Antarctic Cold Reversal (BA/ACR, 15-13 kyr), atmospheric

80   CO_2 concentrations plateau at 240 ppm, but display a slightly increasing $\delta^{13}C_{atm}$ (Fig. 1), potentially

81   the result of circulation changes in the Southern Ocean and/or regrowth of the terrestrial biosphere

82   (Schmitt et al., 2012, Bauska et al., 2016). This plateau is followed by a second rise in atmospheric

83   CO_2 and a concomitant decrease in $\delta^{13}C_{atm}$ during the YD (12.9-11.5 kyr; Fig. 1). This is proposed to

84   have been driven by a combination of the loss of terrestrial organic carbon, a renewal of upwelling in

85   the Southern Ocean, and rising ocean temperatures (Bauska et al., 2016). Some proxy evidence

86   indicates that circulation-driven changes in the efficiency of the biological carbon pump in the

87   Southern Ocean contributed to this second atmospheric CO_2 increase during the YD (Anderson et al.,

88   2009, Skinner et al., 2014), whilst other datasets show a more muted response (Spero and Lea,

89   2002, Skinner et al., 2010, Burke and Robinson, 2012, Roberts et al., 2016; Fig. 1).

90   The modern Southern Ocean acts primarily as a carbon sink (Fig. 2), accounting for approximately

91   40% of global oceanic uptake of anthropogenic CO_2 (DeVries, 2014). There is however significant

92   spatial variability in this flux, most notably as the result of upwelling of CO_2-rich subsurface water at

93   the Antarctic Polar Front (Takahashi et al., 2012; Fig. 2). Reconstructions of Southern Ocean CO_2

94   outgassing over the last deglacial would provide important constraints on how the influence of

95   various mechanisms proposed to drive deglacial CO_2 rise evolved (Galbraith and Skinner, 2020). Such

96   reconstructions can be ascertained from planktic foraminifera $\delta^{11}B$ records, however there are

97   currently only a few that directly and quantitatively assess the CO_2 flux in the Southern Ocean over

98   the last deglaciation (Martinez-Boti et al., 2015, Moy et al., 2019). Some of these do not cover the

99   entire 20 kyr period (Martinez-Boti et al., 2015), while those that do are located in the Sub-Tropical

100   Frontal Zone (STFZ) on the edge of the Southern Ocean (Moy et al., 2019). Here we present new

101   boron isotope ($\delta^{11}B$) analyses of planktic foraminifera *Globigerina bulloides* to determine the sea

102   surface CO_2 flux from the Sub-Antarctic Atlantic and Sub-Antarctic Pacific of the Southern Ocean

103   across the entire glacial termination for the first time, and thus further provide additional

104   constraints on the mechanisms of atmospheric CO_2 rise.

105   **2. Methods and Materials**

106   **2.1. Samples**

107   The samples used in this study come from two sediment cores covering the last 20 kyr. The first core

108   site (TAN1106-28; 48.372°S, 165.659°E) is located in the northern part of the Solander Trough, south

109   of New Zealand at a water depth of 2798 m. The second core site lies on the southern flank of the

110   Agulhas Ridge in the Sub-Antarctic Atlantic (Piston Core TTN057-6-PC4 (ODP1090); 42°54.5'S, 8°54.0'E)

111   at a water depth of 3702 m. Today, site ODP1090 is situated just north of the Sub-Antarctic Front, the

112   boundary between the AZ and the SAZ, where intermediate waters are formed. Site TAN1106-28 is

113   located on the boundary between SAZ and STFZ, however during the last glacial and deglacial period

114   it is reasoned, based on low productivity and temperatures, that the STFZ shifted northwards within

115   the Solander Trough, thus this core site predominantly records the evolution of Sub-Antarctic surface

116   waters (Bostock et al., 2015). Both sites are located above the modern carbonate lysocline and do not

117   appear to be influenced by dissolution through our study interval (Venz and Hodell, 2002, Bostock et

118   al., 2011).

119   **2.2. Age Model for TAN1106-28 and ODP1090**

120   The age model for TAN1106-28 is based on seven ^{14}C dates of mixed planktic (predominantly *G.*

121   *bulloides*) foraminifera and three $\delta^{18}O_{G.\ bulloides}$ tie points based on the alignment with the EPICA Dome

122   C δD record using the AICC2012 chronology (Fig. S1). Three of the ^{14}C dates were previously published

123   in Bostock et al. (2015). A core top age of 1000 years with a ±500 year uncertainty was assumed.

124   Following Skinner et al. (2015), reservoir correction ages of 400 yr (<15 kyr) and 1000 yr (>15 kyr) were

125   applied. To assess the influence of reservoir age on the age uncertainty different combinations (0 yr,

126   400 yr, 1000 yr) were explored, but these showed no significant impact on the age model (Fig. S1).

127   The agreement of the Mg/Ca$_{G.bulloides}$ sea surface temperature with the EPICA Dome C δD record

128   provides good support for this age model, and all age model uncertainty is incorporated into the

129   calculation of ΔpCO_2.

130   The age model for ODP1090 is based on nine new ^{14}C dates measured on *G. bulloides* (Fig. S2). As in

131   Martinez-Boti et al. (2015) a varying reservoir age of 300 yr (<16 kyr) and 900 yr (>16 kyr) was applied,

132   but constant reservoir ages of 0 yr, 300 yr, and 900 yr were also used to assess the impact that

133   reservoir age uncertainty bears on the age model. Comparison of both the Mg/Ca$_{G.bulloides}$ sea surface

134   temperature to the EPICA Dome C δD record and of the ODP1090 $\delta^{15}N_{G.bulloides}$ of Martínez-García et

135   al. (2014) to the nearby Sub-Antarctic zone coral $\delta^{15}N$ record of Wang et al. (2017), which is

136   independently dated using U-Th and ^{14}C ages provides good support for the robustness of this age

137   model (Fig. S2). As in the TAN1106-28 record, age model uncertainty is propagated into the calculation

138   of ΔpCO_2.

139   All radiocarbon data were calibrated using SHCal13 (Hogg et al., 2016), and the age models were

140   generated using the 'UndaTable' MATLAB software (Lougheed and Obrochta, 2019) which ran 10,000

141   Monte Carlo simulations using bootstrapping at 30% and a sediment rate uncertainty of 0.1.

2.3. Trace Element and Boron Isotopic Analysis

Twenty-three samples from ODP1090 and fourteen from TAN1106-28, were analysed for Mg/Ca and δ^{11}B at a temporal resolution of 1 kyr and 1.5-2 kyr, respectively. Sediment samples were washed with Milli-Q (>18 MΩcm) over 63 μm sieves and dried in an oven at 50 °C. Sufficient *Globigerina bulloides* individuals from the 180-355 μm (700 individuals), 250-355 μm (500 individuals) or 300-355 μm (300 individuals) size fractions were picked to reach a minimum sample size of ~4 mg of foraminiferal carbonate (equivalent to ~15 ng B). The narrower size fraction range was favoured when possible and was achieved in 75% of samples. Where possible, all size fractions were picked and run as separate samples to investigate the variability between them (Fig. S3). Despite slightly different δ^{11}B values in the measured size fractions, a consistent offset was not evident and most were within analytical uncertainty, thus combining size fractions when required will not affect derived CO_{2sw} interpretations. Samples were prepared and cleaned for trace element and boron isotope analysis following the method described by Henehan et al. (2015). Trace element analysis was performed on a ThermoScientific Element 2 ICP-MS at the University of Southampton using the method described by Henehan et al. (2015). Long-term reproducibility of Mg/Ca and Al/Ca ratio measurements were 4.5% and 25% (2σ) respectively, based on repeat measurements of in-house consistency standards. As Al/Ca is only used to ensure samples had been cleaned sufficiently to remove clay contamination this relatively large uncertainty does not affect the data presented here.

Boron was isolated from the sample matrix via column separation using the ion exchange resin Amberlite IRA-743 (Kiss, 1988). This resin was loaded onto 20 μL Teflon columns, which contained a 3.8 mm diameter polyethylene frit with a pore size of 10-30 μm. These columns were thoroughly cleaned with Teflon distilled 0.5 M HNO_3 and rinsed with 18.2 MΩcm Milli-Q prior to use. The performance of each new column was rigorously tested with a set of reference materials prior to use (NIST SRM 951, JCp-1, and NIST RM 8301f (Stewart et al.)). Since the boron retention of Amberlite IRA-743 is pH dependent, samples were buffered to ≥ pH 5 using a 2M Na-acetate 0.5M acetic acid

167 buffer prior to loading. At pH 5 the resin has a boron partition coefficient of ~10^4 and this allows

168 sufficiently rapid adsorption of boron onto the column for quantitative recovery (Lemarchand et al.,

169 2002). To avoid overloading the columns with ions, the volume of buffer added to the sample was

170 minimised to an upper limit of 600 μl. The buffered samples were then loaded onto the columns in

171 200 μL aliquots to avoid building up a large hydrostatic head that preliminary data showed was

172 associated with isotopic fractionation due to overly rapid transit time through the column. The

173 matrix was then removed by rinsing with eight separate elutions of 200 μL of Milli-Q, ensuring the

174 walls of the column were well-rinsed. Finally, the sample was eluted by adding 110 μL of 0.5M HNO_3

175 in five aliquots to ensure all boron was collected. A sixth aliquot was collected separately by loading

176 a final 110 μL of 0.5M HNO_3 and was analysed to confirm boron elution was complete. Isotopic

177 analysis was performed on a ThermoScientific Neptune MC-ICPMS at the University of Southampton

178 following the methods of Foster (2008) and Foster et al. (2013). Reproducibility was calculated based

179 on the relationship between intensity and external reproducibility of repeat analysis of JCp-1

180 following Rae et al. (2011); typical uncertainty for a 20 ppb sample was 0.20 ‰ at 2σ.

181 **2.4. Carbonate System Calculations**

182 To calculate pH, a species specific calibration needs to be applied to convert measured $\delta^{11}B_{Calcite}$ to

183 $\delta^{11}B_{Borate}$ (Foster and Rae, 2016). *G. bulloides* is symbiont barren so the pH of its microenvironment is

184 lower than that of ambient seawater (Henehan et al., 2016). The $\delta^{11}B_{Calcite}$ - $\delta^{11}B_{Borate}$ calibration used

185 (Raitzsch et al., 2018; Eq. 1) is based on the relationship between plankton tow and core top data

186 (Martínez-Botí et al., 2015, Raitzsch et al., 2018) to $\delta^{11}B_{Borate}$ derived from seasonally resolved

187 carbonate system parameters.

188 Eq. 1:
$$\left(\delta^{11}B_{Borate} = \frac{(\delta^{11}B_{Calcite} + 3.58 \pm 11.77)}{1.09 \pm 0.65} \right)$$

189 These values were used in conjunction with temperature and salinity estimates to calculate pH and

190 CO_{2sw} (Foster and Rae, 2016). Sea surface temperatures (SST) were derived from the measured Mg/Ca

191   on the same samples used for $\delta^{11}B$, using the calibration of Elderfield and Ganssen (2000). Salinity was

192   calculated accounting for the decrease due to ice sheet melt over the deglacial transition as in Palmer

193   and Pearson (2003). A Monte Carlo approach, which randomly selects input parameters within their

194   2σ uncertainty range was used to produce 10,000 realisations of $\delta^{11}B_{Borate}$, pH and CO_{2sw} to fully

195   propagate uncertainty. These input parameters include (at 2σ) Mg/Ca SST: ±1.8 ^oC, salinity: ±0.5 psu,

196   and $\delta^{11}B_{Calcite}$: dependent on analysis, but typically ±0.2-0.4 ‰. The $\delta^{11}B$ derived CO_{2sw} record was

197   smoothed by plotting a three point running mean based on a 500 year interpolation of the CO_{2sw}

198   values. The uncertainty is displayed for each data point as the 2.5[th], 16th, 84th, and 97.5[th] percentiles

199   of the Monte Carlo realisations (Fig. 3). Due to the close relationship between change in aqueous CO_2

200   and change in pH, it is argued that surface ocean pH change is the dominant driver of surface water

201   CO_2 change (Hain et al., 2018). The error associated with defining the second carbonate parameter

202   (alkalinity) in these calculations is therefore not propagated into estimates of CO_{2sw} here (Hain et al.,

203   2018). The above calculations were performed using the 'seacarb' package in R. To determine the role

204   of the Sub-Antarctic Atlantic and Pacific as a source of CO_2 to the atmosphere, ΔpCO_2 was calculated

205   using the contemporaneous CO_{2atm} from the ice core CO_2 record (Bereiter et al., 2015; Eq. 2; Figs. 1,

206   4):

207   Eq. 2: $\Delta pCO_2 = CO_{2sw} - CO_{2atm}$

208   When estimating ΔpCO_2, age model uncertainty was propagated using a second Monte Carlo

209   approach. A positive ΔpCO_2 indicates outgassing where the surface ocean around the core site

210   location acted as a source of CO_2 to the atmosphere, whilst a negative ΔpCO_2 indicates the surface

211   ocean was a net sink of CO_2 from the atmosphere. These new boron isotope derived ΔpCO_2 records

212   from the Sub-Antarctic Pacific and Sub-Antarctic Atlantic are then presented alongside a global

213   compilation of published records to explore spatial variability in carbon outgassing from the surface

214   ocean over the deglaciation (Fig. 5). All of these records, and the associated uncertainties, are based

215   on the published pCO_{2sw} data. Error bars vary significantly across these datasets depending on the

216   analytical approach and uncertainty propagation undertaken and reported in each study. In the

217   cases of AA59/1 (Naik et al., 2015) and PC75-2 and PC83-1 (Shao et al., 2019), uncertainty associated

218   with the pCO$_{2sw}$ values were not reported and so a typical uncertainty of ±25 ppm has been applied.

2.5. Carbon Isotopic Analysis

220   From ODP1090 δ^{13}C analysis was undertaken every 1 kyr on the planktic foraminifera *G. bulloides*.

221   Twenty individuals from the 300-355 μm size fraction were picked and cracked open individually.

222   Samples were rinsed with methanol, ultrasonicated for 5 seconds, and left at room temperature to

223   dry. Stable isotopic analyses were performed on a Thermo Finnigan MAT253 coupled with a Kiel IV

224   carbonate device at the University of Southampton. A two-point calibration using international

225   standards NBS 18 and NBS 19 was used to correct to Vienna PeeDee Belemnite (VPDB), the standard

226   deviation based on in-house carbonate standard GS-1 is 0.02 ‰ (1σ). Oxygen and carbon stable

227   isotopes on *G. bulloides* were previously published for TAN1106-28 (Maxson et al., 2019).

2.6. Alkenone Analysis

229   Analysis and characterization of total lipid content for samples from site TAN1106-28 with a

230   temporal resolution of 1-1.5 kyr were performed at Institut de Ciències del Mar in Barcelona

231   following published methods (Villanueva et al., 1997, Calvo et al., 2003, Kornilova and Rosell-Melé,

232   2003). Briefly, 3-4 g of freeze-dried sediment were loaded into 20 ml Teflon extraction vessels of a

233   MARS6 microwave digestion system (CEM). After addition of internal standards (hexatriacontane

234   and nonadecanol) and subsequent extraction with a dichloromethane/methanol mixture (3:1), the

235   extracts (~ 15 ml) were evaporated to dryness under a gentle nitrogen stream. 6% potassium

236   hydroxide in methanol was used to hydrolyze wax esters and eliminate interferences during

237   quantization of gas chromatographic data. After derivatization with

238   bis(trimethylsilyl)trifluoroacetamide, extracts were dissolved in toluene and then injected in an

239   Agilent 7890 Gas Chromatograph with a flame ionization detector and equipped with a HP-1

240   capillary column (60 m, 0.25 mm I.D. and 0.25 μm film thickness). H$_2$ was used as carrier gas. The

241   oven was programmed from 90 °C (holding time of 1 min) to 190 °C at 20 °C/min, then to 290 °C at 6

242   °C/min with a 40 min hold at 290 °C and finally, from 290 °C to 310 °C at 10 °C/min with a holding

243   time of 6 min. The reproducibility of the analytical methodology was tested with a homogenous

244   sediment standard, which gave analytical errors of 15% in the determination of alkenone

245   concentration.

246   The vertical flux of alkenones were corrected for redistribution on the ocean floor using U-series

247   analysis of the same sediment samples (Trudgill et al., Submitted) utilising the ^{230}Th-normalisation

248   approach (Francois et al., 2004, Costa et al., 2020; Eq. 3). Here the expected production of ^{230}Th in

249   the water column (β_{230} x z [depth]) is divided by the measured concentration of ^{230}Th, corrected for

250   decay, (^{230}Th$_{xs,0}$). To determine alkenone flux (F_i), the vertical particle flux value was multiplied by the

251   measured alkenone concentrations (c_i).

252   Eq. 3: $$F_i = \frac{C_i \times \beta_{230} \times z}{^{230}Th_{xs,0}}$$

253   **3. Results**

254   TAN1106-28 records glacial *G. bulloides* boron isotope values of 16.0 ‰, which corresponds to a sea

255   surface pH of 8.25 (Fig. 3). The record from Site ODP1090 exhibits glacial values of 16.5 ‰, which

256   corresponds to a sea surface pH of 8.3. They both present significant negative δ^{11}B excursions

257   around HS1 when TAN1106-28 declines to 15 ‰ (pH 8.15) and site ODP1090 declines to 15.5 ‰ (pH

258   8.2). At site TAN1106-28, the boron isotope record returns to pre-excursion values (pH 8.25) at 12

259   ka (Fig. 3), which is comparable to the ODP1090 record, which returns to pre-excursion boron

260   isotopic values (~16.2 ‰) at 15 ka. Both records then hover around 16 ‰, with significant variability

261   of ±0.5 ‰ (pH 8.1-8.25; Fig. 3) until the core top. Both Mg/Ca SST records display an increase of ~5-6

262   °C from 19-12 kyr (Fig. 3); Site TAN1106-28 displays glacial SST values of 8 °C, which increase steadily

263   to 14 °C between 19-11 kyr while Site ODP1090 records slightly cooler temperatures of around 7 °C

264   in the glacial, which increase steadily from 19-13 kyr to 12 °C where they stabilise (Fig. 3). Boron

265 isotope derived CO_{2sw} records from TAN1106-28 show glacial CO_{2sw} concentrations around 240 ppm,

266 slightly higher than atmospheric levels from the ice cores, whilst the ODP1090 CO_{2sw} reconstructions

267 are ~200 ppm, similar to the contemporaneous atmospheric CO_2 (Fig. 3). During HS1, from 17-13 kyr,

268 sites TAN1106-28 and ODP1090 show an increase in ΔpCO_{2sw} of up to 100 ppm and 50 ppm,

269 respectively (Fig. 4). From 13 kyr to the end of the deglaciation, reconstructed CO_{2sw} values from site

270 TAN1106-28 and ODP1090 remain similar to atmospheric levels (Fig. 3).

271 The alkenone concentrations from site TAN1106-28 (this study) and ODP1090 (Martínez-García et

272 al., 2014) declined from 4000-1000 ng/cm^2/kyr and 450 ng/cm^2/kyr to very low values, respectively,

273 immediately prior to the onset of HS1 (17.5-15 kyr), and then remain stable (Fig. 4). At both sites

274 $\delta^{13}C_{G.bulloides}$ show a similar overall pattern of a decline in the early deglacial with a gradual recovery

275 during the Holocene (Fig. 4). However, while the $\delta^{13}C_{G.bulloides}$ from site TAN1106-28 declines

276 throughout HS1, the $\delta^{13}C_{G.bulloides}$ record from site ODP1090 reaches a peak during HS1 and then

277 subsequently decreases.

278 Comparison of these new ΔpCO_2 records from the Sub-Antarctic Pacific and Sub-Antarctic Atlantic to

279 a global compilation of all existing $\delta^{11}B$ derived ΔpCO_2 records highlights the spatial and temporal

280 heterogeneity of CO_2 outgassing from the surface ocean over the last deglacial (Fig. 5). Whilst each

281 record is influenced by regional processes and is therefore unique to its particular location, they can

282 be compared to provide insights into the mechanisms of CO_2 transfer from the ocean subsurface to

283 the atmosphere during the deglacial, and subsequent atmospheric CO_2 rise, as discussed in the

284 following section.

285 **4. Discussion**

286 **4.1. Deglacial Southern Ocean ΔpCO_2**

287 During the last glacial period (>18 kyr) site TAN1106-28 was characterised by surface water CO_{2sw}

288 concentrations of ~240 ppm, making it a source of CO_2 to the atmosphere (Fig. 3, 4). This is

289 interpreted to be the result of frontal migration in this region, during the glacial this site would have

290 been located further in the SAZ, whereas today it is influenced by the highly productive STFZ

291 (Bostock et al., 2015), which would reduce the pre-industrial ΔpCO_2. At ODP1090, there is only one

292 data point from the very late glacial, which suggests this site may have been a minor source of CO_2

293 to the atmosphere (<20 ppm; Fig. 4). In comparison, the ΔpCO_2 record from core MD97-2106,

294 located south of Tasmania (Moy et al., 2019; Fig. 5), suggests that the Sub-Antarctic was neither a

295 source nor a sink of CO_2 during the glacial. At the start of the deglacial transition (HS1; 18-15 kyr),

296 there was an increase in ΔpCO_2 at both Sub-Antarctic Pacific (TAN1106-28) and Atlantic (ODP1090)

297 sites. These regions of the Southern Ocean became much larger sources of CO_2 to the atmosphere at

298 this time, with ΔpCO_2 values of 100 ppm and 50 ppm, respectively (vs. 20 ppm and -20 ppm today

299 respectively; Fig. 4). These ΔpCO_2 values are similar to changes reported from other regions of the

300 Southern Ocean (Fig. 5) with increases of 50-150 ppm CO_2 evident from Sub-Antarctic Atlantic site

301 PS2498 (Martinez-Boti et al., 2015), and Pacific STFZ sites PC75-2, and PC83-1 (Shao et al., 2019). The

302 current explanation for this shift to carbon source is a reduction in stratification of the deep

303 Southern Ocean (Skinner et al., 2010, Rae et al., 2018) and enhanced upwelling in the AZ (Anderson

304 et al., 2009, Studer et al., 2015). This would have resulted in an enhanced supply of nutrients and

305 light carbon (low $\delta^{13}C$) to the surface waters of the Southern Ocean (Spero and Lea, 2002, Ziegler et

306 al., 2013). This was combined with a decline in biological productivity and efficiency of the carbon

307 pump in the SAZ due to the reduction in dust supply (Lambert et al., 2012, Lamy et al., 2014,

308 Martínez-García et al., 2014, Galbraith and Jaccard, 2015). Comparison to the $\delta^{15}N_{G.\ bulloides}$ record at

309 ODP1090 further supports this assertion as the coeval decrease in $\delta^{15}N$ with ΔpCO_2 (Fig. 1) indicates

310 that a reduction in nutrient utilisation resulted in excess surface water pCO_2 (Martínez-García et al.,

311 2014). This is entirely consistent with the observed decline in alkenone fluxes and planktic $\delta^{13}C$

312 around 18-12 kyr we observe at TAN1106-28 and ODP1090 (Fig. 4).

313 In contrast, the waters south of Tasmania (site MD97-2106) remained a minor sink of CO_2 during HS1

314 (Moy et al., 2019; Fig. 5). The observed discrepancy between sites in the southwest Pacific (MD97-

315 2106 and TAN1106-28; Fig. 5) is interpreted to be the result of the relative location of these two

316 sites with respect to Antarctic upwelling and the scale by which the AZ upwelling signal can be

317 affected by SAZ productivity. For example site TAN1106-28 was located south of the STFZ during the

318 last glacial and deglacial, whilst MD97-2106 remained within the STFZ. Thus, similar to the modern

319 ocean, there was considerable variability in CO_2 flux across the Southern Ocean with the possibility

320 that during the deglacial ΔpCO_2 also decreased northwards from the SAZ towards the STFZ, as it

321 does today (Fig. 2).

322 The BA/ACR is characterised by an initial rapid increase in atmospheric CO_2 by ~10 ppm over a few

323 hundred years, followed by sustained atmospheric CO_2 levels between 14.7-12.7 kyr (Bereiter et al.,

324 2015). The records from this study show that the CO_2 content of surface waters from the Sub-

325 Antarctic Pacific (TAN1106-28) are still in decline (notwithstanding our relatively low sample

326 resolution), while surface waters from the Sub-Antarctic Atlantic (ODP1090) returned to

327 contemporaneous atmospheric levels during the BA/ACR (Fig. 4). This, accompanied by low alkenone

328 fluxes at both of these sites, indicates that despite low biological productivity, only negligible

329 amounts of CO_2 were being released in the Sub-Antarctic during the BA/ACR (Fig. 4). This perhaps

330 reflects the dominant control AZ upwelling, and the location of the SAZ site relative to this upwelling

331 signal bears on the ΔpCO_2 recorded at the site. The $\delta^{15}N_{G.bulloides}$ record from ODP1090 shows no

332 major change over this period (Fig. 1), which may reflect how AZ upwelling has a greater control on

333 ΔpCO_2, whilst local biological productivity has a more dominant influence on nutrient consumption,

334 and hence on $\delta^{15}N$ (Martínez-García et al., 2014). At TAN1106-28 the planktic $\delta^{13}C$ stabilised

335 following the decline of HS1, whilst at ODP1090 the planktic $\delta^{13}C$ continues to decline, perhaps

336 reflecting low biological productivity during this period (Fig. 4).

337   These new ΔpCO_2 values are in agreement with the record from site MD97-2106, south of Tasmania

338   (Moy et al., 2019), whilst PS2498 in the Sub-Antarctic Atlantic, west of ODP1090, shows variable flux

339   of ΔpCO_2 of up to 40 ppm throughout this period (Martinez-Boti et al., 2015). Despite this, there is

340   evidence for an overall decrease in ΔpCO_2 of the Sub-Antarctic during the BA/ACR (e.g. surface

341   waters closer to atmospheric equilibrium). This can be explained by a reduction in upwelling of

342   isotopically light carbon and nutrient rich waters in the AZ (Anderson et al., 2009; Fig. 1) and is

343   reflected in the recovery of $\delta^{13}C_{atm}$ (Schmitt et al., 2012, Bauska et al., 2016; Fig. 1).

344   The onset of the YD is associated with the second major increase (30 ppm) in atmospheric CO_2 and a

345   second decline in $\delta^{13}C_{atm}$ (Schmitt et al., 2012, Bauska et al., 2016; Fig. 1). The boron isotope derived

346   ΔpCO_2 records from the Sub-Antarctic Pacific (TAN1106-28) show that this region was transitioning

347   to a minor sink of CO_2 (although we have limited sample resolution during this interval; Fig. 4).

348   Similarly, the Sub-Antarctic Atlantic (ODP1090) record shows no significant evidence that this region

349   was a major source of CO_2 during this period. The alkenone fluxes from both these locations also

350   remained low throughout the YD (Fig. 4). Although there is a decrease in $\delta^{15}N_{G.bulloides}$ over this

351   period, this is also decoupled from a change in alkenone flux. Consequently Martínez-García et al.

352   (2014) suggest that other influences besides iron fertilisation may affect the $\delta^{15}N_{G.bulloides}$ record

353   during this episode, and so the lack of correlation between the $\delta^{15}N$ and $\delta^{11}B$ derived ΔpCO_2 may

354   not be contradictory. As noted above, the apparent heterogeneity observed in ΔpCO_2 records across

355   the Southern Ocean during the YD also likely reflects that ΔpCO_2 is a combined signal of both AZ

356   upwelling and SAZ productivity and that this variability occurs due to the location of the core site

357   with respect to AZ upwelling. The agreement of the PS2498 ΔpCO_2 record with AZ upwelling

358   (Anderson et al., 2009), but lack of correlation with productivity records from PS2498 itself

359   (Anderson et al., 2014) suggests that this site records a relatively pure AZ signal. Conversely the

360   other Sub-Antarctic Atlantic site ODP1090, which is located further away from Antarctic upwelling,

361   appears to reflect a signal more dominated by the SAZ, especially during the second part of the

362   deglacial. Similarly in the Pacific sector, the lack of any evidence for CO_2 outgassing from site MD97-

363   2416 (Moy et al., 2019) suggests that the sedimentary archive is recording a mixed STFZ and SAZ

364   signal, whilst TAN1106-28 has more of a AZ influence.

365   Radiocarbon data suggests that the majority of upwelling of deep water carbon had stopped by 15

366   ka in the Atlantic sector of the Sub-Antarctic (Skinner et al., 2010, Burke and Robinson, 2012; Fig, 1).

367   Furthermore, during the YD, planktic $\delta^{13}C$ values are still low, possibly reflecting a combination of

368   continued low productivity in the region as evidence by low alkenone fluxes, continued upwelling

369   further south in the AZ, and top-down atmospheric forcing (Fig. 4). The lack of evidence for

370   widespread and significant outgassing of carbon from the Sub-Antarctic during the YD suggests that

371   sources of CO_2 outside of the Sub-Antarctic ocean drove the second rise in atmospheric CO_2.

372   Previous studies using $\delta^{13}C_{atm}$, concluded that the CO_2 rise during the YD was primarily associated

373   with a further weakening of the oceanic biological carbon pump due to upwelling in response to an

374   enhancement of the Southern Hemisphere Westerlies alongside oceanic warming (Bauska et al.,

375   2016). The results of this study indicate that the flux of CO_2 from the surface ocean into the

376   atmosphere associated with the enhanced upwelling as evidenced by Anderson et al. (2009) and

377   Studer et al. (2015) must have been limited spatially within the AZ.

378   ### 4.2. **Deglacial ΔpCO_2: A Global Perspective**

379   The Sub-Antarctic was not the only location during HS1 where there was significant flux of CO_2 from

380   the surface ocean to the atmosphere. As reviewed by Shao et al. (2019), global records of ΔpCO_2

381   (Fig. 5) show an enhanced flux of CO_2 from the ocean to the atmosphere during HS1 in the

382   Equatorial Pacific (Palmer and Pearson, 2003, Martinez-Boti et al., 2015), the upwelling regions of

383   the Eastern Equatorial Atlantic (Foster and Sexton, 2014), the North Pacific (Gray et al., 2018), and

384   the North Atlantic (Norwegian Sea) (Ezat et al., 2017). The ΔpCO_2 signature observed in the

385   upwelling regions of the low latitudes is interpreted to be the downstream expression of the Sub-

386   Antarctic surface waters, which are subducted in the SAZ to form intermediate waters (Toggweiler,

387   1999, Sarmiento et al., 2004, Martinez-Boti et al., 2015). These intermediate depth waters are

388   upwelled in the Eastern Equatorial Pacific, Eastern Equatorial Atlantic, and Indian Ocean (Toggweiler,

389   1999, Sarmiento et al., 2004). All these low latitude sites also show a decline in planktic $\delta^{13}C$, which

390   has been attributed to either an increase in local upwelling and/or a change in the signature of the

391   source water that is upwelled (Ninnemann and Charles, 1997). Alternatively, this depleted $\delta^{13}C$

392   signal, which is also evident in the $\delta^{13}C_{atm}$ recorded by ice cores, may have been transferred through

393   the atmosphere (Spero and Lea, 2002). The consistent timing of an increase in ΔpCO_2 with a decline

394   in the $\delta^{13}C$ recorded in ice-cores and planktic foraminifera during the deglaciation observed in this

395   study and in others indicates that an increase in upwelling of $\delta^{13}C$ depleted waters must play an

396   important role.

397   The increase in ΔpCO_2 from the Norwegian Sea during HS1 (JM-FI-19PC; Ezat et al., 2017) is

398   accompanied by a decrease in planktic $\delta^{13}C$ and an increase in the nutrient concentration proxy

399   Cd/Ca. This is, however, not associated with upwelling of old deep water, as the radiocarbon record

400   at this site indicates younger surface water at this location around 16.5 ka. The enhanced CO_2

401   concentration at the surface in this case has been interpreted to be the result of either a decrease in

402   biological productivity, rejection of CO_2-rich brine during sea ice formation, the signature of water

403   higher in CO_2 inflowing from the low latitude Atlantic, or a slowdown of deep water formation,

404   leaving carbon to accumulate in the surface waters (Ezat et al., 2017). Conversely, an increased CO_2

405   flux is absent from sites in the Caribbean Sea and the Western Equatorial Atlantic (ODP999, GeoB-

406   1523; Foster and Sexton, 2014) and far Western Equatorial Pacific (KR05-15; Kubota et al., 2019)

407   during HS1. This observed zonal decrease in ΔpCO_2 gradient is suggested to be the result of

408   intensified and extended upwelling in the east and central Equatorial Atlantic and Pacific, which did

409   not expand as far west as ODP999, GeoB-1532, or KR05-15 (Palmer and Pearson, 2003, Foster and

410   Sexton, 2014, Kubota et al., 2019; Fig. 5).

411   During the northern hemisphere BA (southern hemisphere ACR) the North Pacific (MD01-2416),

412   Arabian Sea (AA59/21) and Western Equatorial Pacific (ERDC-92) all show evidence of CO_2

413   outgassing from the surface ocean to the atmosphere (Palmer and Pearson, 2003, Naik et al., 2015,

414   Gray et al., 2018). The North Pacific signal is interpreted to be the result of wind-driven upwelling of

415   CO_2 and nutrient-rich deep water (Galbraith et al., 2007), which continued into the YD (Gray et al.,

416   2018). This is suggested to have led to enhanced export productivity, increased remineralisation of

417   organic carbon at depth, and subsequent widespread hypoxia in the North Pacific Basin (Jaccard and

418   Galbraith, 2012). Although the Arabian Sea records may be due to the enhancement of upwelling in

419   response to an intensification of monsoons during the BA (Naik et al., 2015), its consistency with

420   these other records instead suggest that it was a global feature of the deglacial surface ocean (Fig.

421   5). Despite evidence of CO_2 outgassing from the surface water, there is no millennial-scale increase

422   in atmospheric CO_2 levels during the BA. It is hypothesised that this outgassing counteracted the

423   return to a stratified Southern Ocean during the ACR (Anderson et al., 2009), which would have

424   increased deep ocean CO_2 storage, allowing atmospheric CO_2 to remain elevated throughout the BA

425   (Gray et al., 2018). The YD is the second major period of atmospheric CO_2 rise over the last deglacial.

426   The only evidence from our global compilation of $\delta^{11}B$ ΔpCO_2 of a greater flux between the oceans

427   and the atmosphere during the YD than in the modern day is from the North Pacific (Gray et al.,

428   2018), Eastern Equatorial Pacific (Martinez-Boti et al., 2015), and North Atlantic (Norwegian Sea)

429   (Ezat et al., 2017; Fig. 5). Both the North Pacific and Eastern Equatorial Pacific sites (Martinez-Boti et

430   al., 2015, Gray et al., 2018) show ΔpCO_2 to be up to 100 ppm during the YD, thus indicating they

431   were major sources of carbon to the atmosphere. The carbon flux in the North Pacific is interpreted

432   to derive from upwelling of carbon-rich water associated with the collapse of North Pacific

433   Intermediate Water formation which resulted in a shoaling of the interior ocean carbon reservoir at

434   the onset of the BA (Gray et al., 2018). In the Eastern Equatorial Pacific, the source of the upwelling

435   and associated CO_2 outgassing is interpreted to be predominantly of Sub-Antarctic origin, with some

436   North Pacific influence, transported via the mode waters (Sarmiento et al., 2004, Martinez-Boti et

437   al., 2015, Toggweiler et al., 2019). Based on the new ΔpCO_2 records presented here, the lack of

438   evidence for significant CO_2 outgassing in the Sub-Antarctic Ocean in the regions of mode water

439   formation during the YD suggests that the CO_{2sw} signal of the Eastern Equatorial Pacific is more

440   heavily influenced by the North Pacific than previously considered. The North Atlantic (Norwegian

441   Sea) may have played a role in the atmospheric CO_2 rise of the YD with site (JM-FI-19PC; Ezat et al.,

442   2017) displaying a minor ΔpCO_2 of up to 20 ppm (Fig. 5). This increase in CO_{2sw} is concurrent with an

443   increase in Cd/Ca ratios measured in the planktic foraminifera, indicative of higher nutrient

444   concentrations at this site suggesting greater upwelling.

445   In addition to changes in the terrestrial biosphere that occurred during the YD (Köhler et al., 2005),

446   based on our new records from the Sub-Antarctic and a compilation of published ΔpCO_2 records, we

447   propose that enhanced upwelling of carbon-rich deep water in the North Pacific, and Eastern

448   Equatorial Pacific and possibly in the Southern Ocean AZ, played a dominant role in driving the

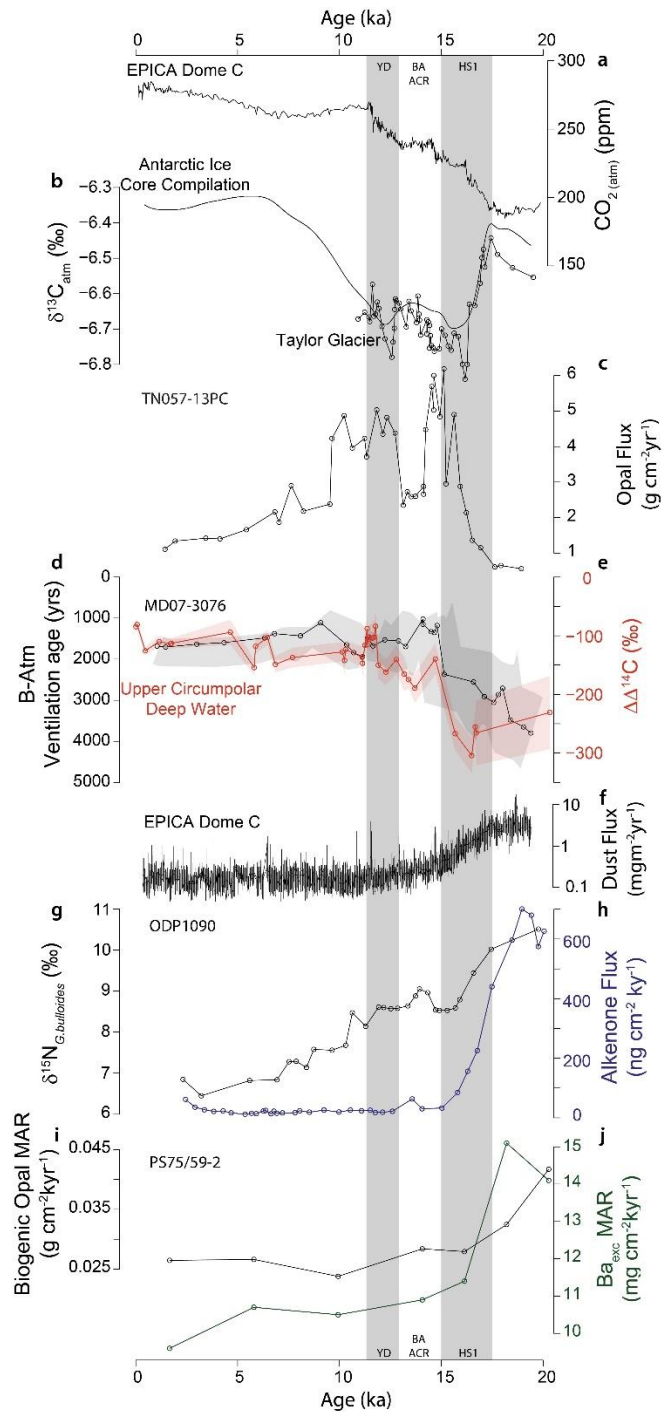449   second rise in atmospheric CO_2.

450   5. **Conclusion**

451   Core sites TAN1106-28 and ODP1090 show evidence of CO_2 outgassing in the Sub-Antarctic Atlantic

452   and Sub-Antarctic Pacific during HS1. In combination with biological productivity (alkenone

453   concentrations), and upwelling proxies ($\delta^{13}C$) this is interpreted to be due to an increase in Southern

454   Ocean upwelling of old, previously sequestered carbon, and a reduction in primary productivity in

455   response to reduced dust-borne iron (Fe) fertilisation. This outgassing is interpreted to have

456   contributed to the initial rise in atmospheric CO_2 of 35 ppm during HS1 observed in the ice core

457   records, although other sites in the Southern Ocean SAZ and STFZ indicate spatial heterogeneity in

458   the CO_2 flux to the atmosphere during HS1, similar to the Southern Ocean today. A global

459   compilation of similar datasets show that this excess CO_2 in the surface waters of the Southern

460   Ocean was transmitted to the low latitudes via intermediate waters where the excess CO_2 is further

461   outgassed to the atmosphere in the eastern parts of the basins via upwelling.

462 Conversely, there is no evidence for the Sub-Antarctic acting as a coherent source of CO_2 from the

463 surface ocean during the second episode of atmospheric CO_2 rise in the YD. The only locations that

464 show significant excess CO_2 during this latter half of the deglacial are the North Pacific and Eastern

465 Equatorial Pacific. We therefore suggest that, whilst the Sub-Antarctic played a key role in driving

466 the initial rise in atmospheric CO_2 during HS1, it was not as significant during the second stage of CO_2

467 rise. However, due to the heterogeneous nature of the Southern Ocean and potential role of the AZ

468 further south, additional records with a greater spatial coverage and higher temporal resolution are

469 required to test this hypothesis.

483

484

Figure 1. Compilation of marine and ice core proxy records over the last 20 kyr. Two episodes of major atmospheric CO_2 rise (Heinrich Stadial 1 (HS1, 17.5-15 kyr) and Younger Dryas (YD, 12.9-11.5 kyr) are highlighted in grey. **a)** Atmospheric CO_2 reconstructions from ice cores (Bereiter et al., 2015). **b)** atmospheric CO_2 $\delta^{13}C$ (‰) from Schmitt et al. (2012) (line) and Bauska et al. (2016) (points). **c)** Opal Flux (g cm^{-2}yr^{-1}), a proxy for upwelling, from Antarctic site TN057-13PC (Anderson et al., 2009). **d)** Deep-water ventilation from core MD07-3076 (B-Atm) (Skinner et al., 2010). **e)** Offset of deep sea coral $\Delta^{14}C$ from contemporaneous atmospheric levels ($\Delta\Delta^{14}C$ (‰)) (Burke and Robinson, 2012). **f)** EPICA Dome C Dust Flux record (Lambert et al., 2012). **h-g)** $\delta^{15}N_{G.bulloides}$ (‰) and alkenone (ng cm^{-2}kyr^{-1}) flux data from Sub-Antarctic site ODP1090 (Martínez-García et al., 2014). **i-j)** Biogenic Opal Mass Accumulation Rate (MAR) (g cm^{-2}kyr^{-1}) and Ba$_{exc}$ MAR (mg cm^{-2}kyr^{-1}) from Sub-Antarctic site PS75/59-2 (Lamy et al., 2014).

496

497

498
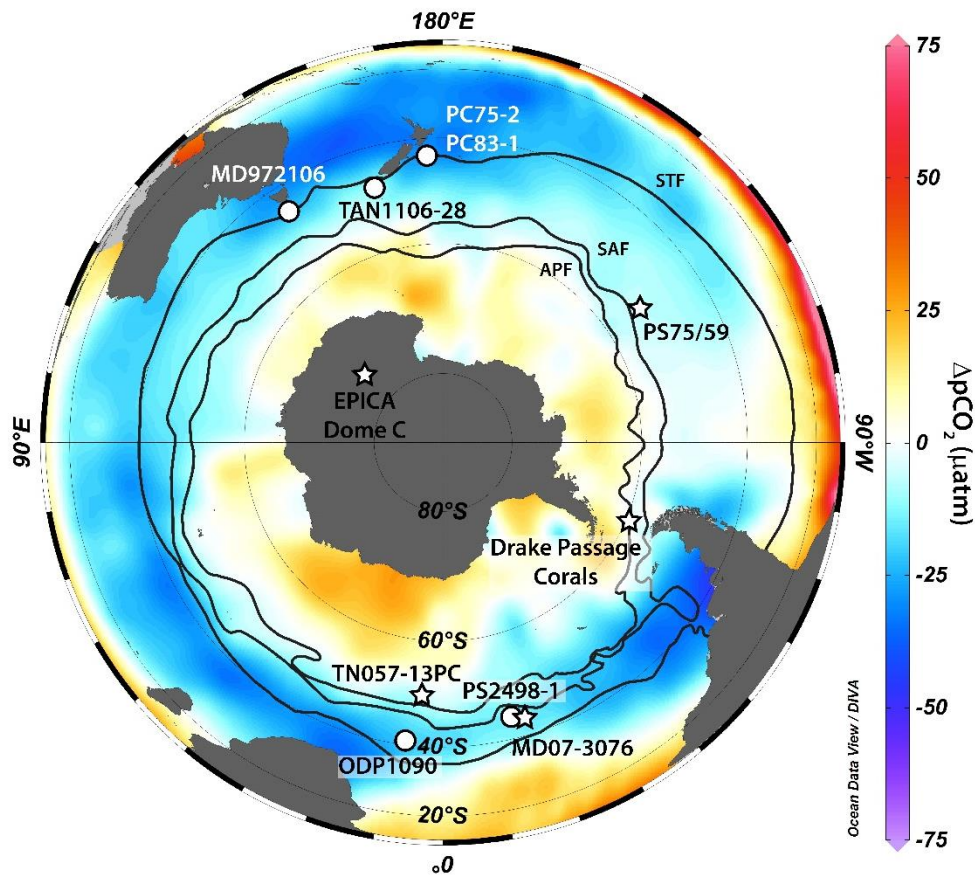
Figure 2. Map of sea surface ΔpCO₂ in the modern Southern Ocean. Warm (red) colours show areas where the ocean is a source of CO₂ to the atmosphere, cold (blue) colours show sink regions. Circles show core locations for boron isotope records referred to in this study, the sites referenced in Fig. 1 are depicted as stars. Black lines depict the Antarctic Polar Front (APF, Sub-Antarctic (SAF) and Sub-Tropical Frontal Zone (STFZ). Made in Ocean Data View (https://odv.awi.de/) using gridded LDEO pCO₂ data of Takahashi et al. (2009) available from (https://odv.awi.de/data/ocean/ldeo-carbon-data/).
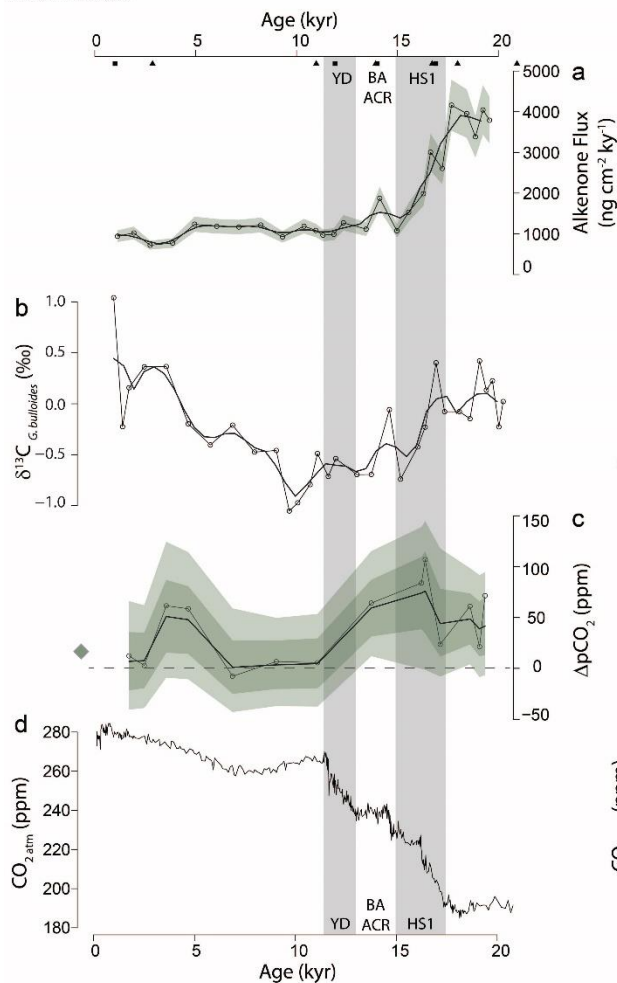
506

507
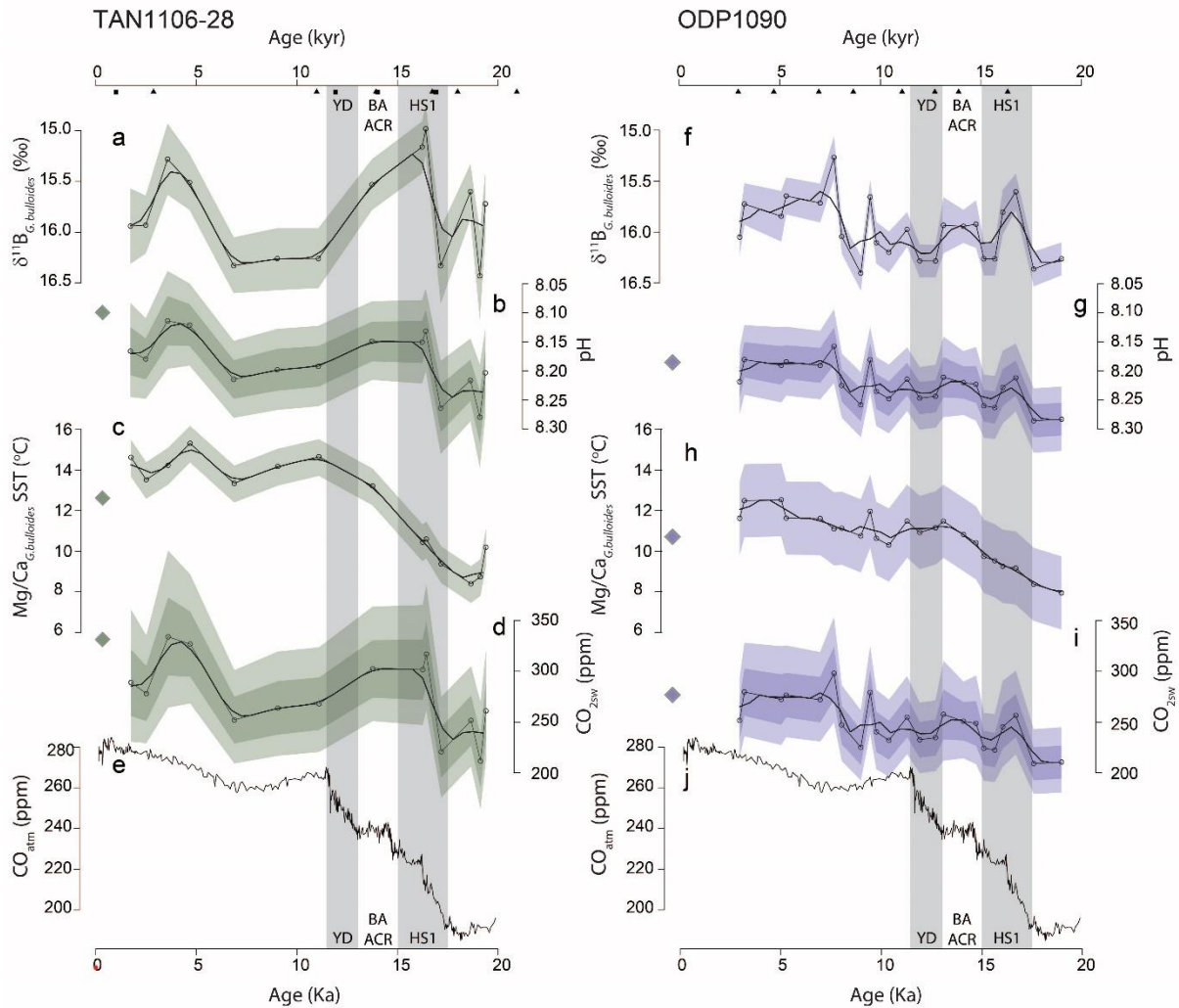
Figure 3. δ^{11}B, pH, SST and CO_{2sw} records from the Sub-Antarctic Pacific (TAN1106-28) and Sub-Antarctic Atlantic (ODP1090) over the last 20 kyr. a-d) Sub-Antarctic Pacific; **f-j)** Sub-Antarctic Atlantic. Two episodes of major atmospheric CO_2 rise (Heinrich Stadial 1 (HS1, 17.5-15 kyr) and Younger Dryas (YD, 12.9-11.5 kyr) are highlighted in grey. Age model ^{14}C ages are displayed as black triangles, and tie points as black squares. Modern pH, SST and CO_{2sw} values at each site are displayed as diamonds. Bold black line represents the running mean of a 500 year interpolation. **a & f)** δ^{11}B$_{G.bulloides}$ (‰) with analytical uncertainties (2σ). **b & g)** δ^{11}B$_{G.bulloides}$ derived pH reconstruction with shaded 68% and 95% uncertainty bands, black line shows calculated equilibrium pH based on atmospheric CO_2. **c & h)** Mg/Ca$_{G.bulloides}$ based sea surface temperature (SST) record with uncertainty margin used within the uncertainty propagation to calculate CO_{2sw}. **d & i)** δ^{11}B$_{G.bulloides}$ derived CO_{2sw} with shaded 68% and 95% uncertainty bands. **e & j)** Atmospheric CO_2 reconstructions from ice cores (Bereiter et al., 2015).
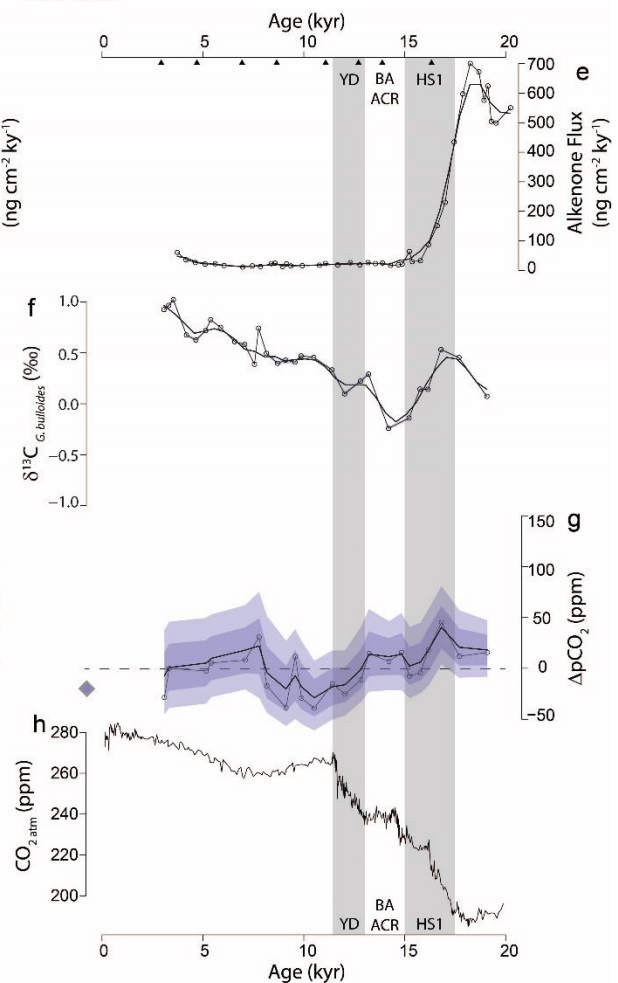
520

521

522

Figure 4. Alkenone flux, $\delta^{13}C_{G.bulloides}$, ΔpCO_{2sw} records from the Sub-Antarctic Pacific (TAN1106-28, a-c) and Sub-Antarctic Atlantic (ODP1090, e-g), and atmospheric CO_2 from ice cores (d & h). Two episodes of major atmospheric CO_2 rise (Heinrich Stadial 1 (HS1, 17.5-15 kyr) and Younger Dryas (YD, 12.9-11.5 kyr) are highlighted in grey. Age model ^{14}C ages are displayed as black triangles, and tie points as black squares. Modern ΔpCO_2 values at each site are displayed as diamonds. Bold black line represents the running mean of a 500 year interpolation. **a)** ^{230}Th normalised alkenone abundance (this study). **b)** TAN1106-28 $\delta^{13}C_{G.bulloides}$ from Maxson et al. (2019). **c)** $\delta^{11}B_{G.bulloides}$ derived ΔpCO_2 with 68% and 95% uncertainty envelopes. **e)** ^{230}Th normalised alkenone flux to site ODP1090 (Martínez-García et al., 2014). **f)** ODP1090 $\delta^{13}C_{G.bulloides}$ (this study) **g)** $\delta^{11}B_{G.bulloides}$ derived ΔpCO_2 with 68% and 95% uncertainty envelopes (this study). **d & h**, Atmospheric CO_2 reconstructions from ice cores (Bereiter et al., 2015).

534

Non-Upwelling Low Latitudes

ODP999

GeoB-1523

KR05-15

Upwelling Eastern Pacific

ODP1238

Upwelling Equatorial Atlantic

GeoB-1105

North Atlantic

JM-F1-19PC

North Pacific

MD01-2416

Sub-Antarctic Zone

PS2498

ODP1090

MD97-2106

TAN1106-28

Upwelling West Pacific & Arabian Sea

ERDC-92

AA59/21

Sub-Tropical South Pacific

PC75-2

PC83-1

ΔpCO_2 (μatm)

Ocean Data View / DIVA

535
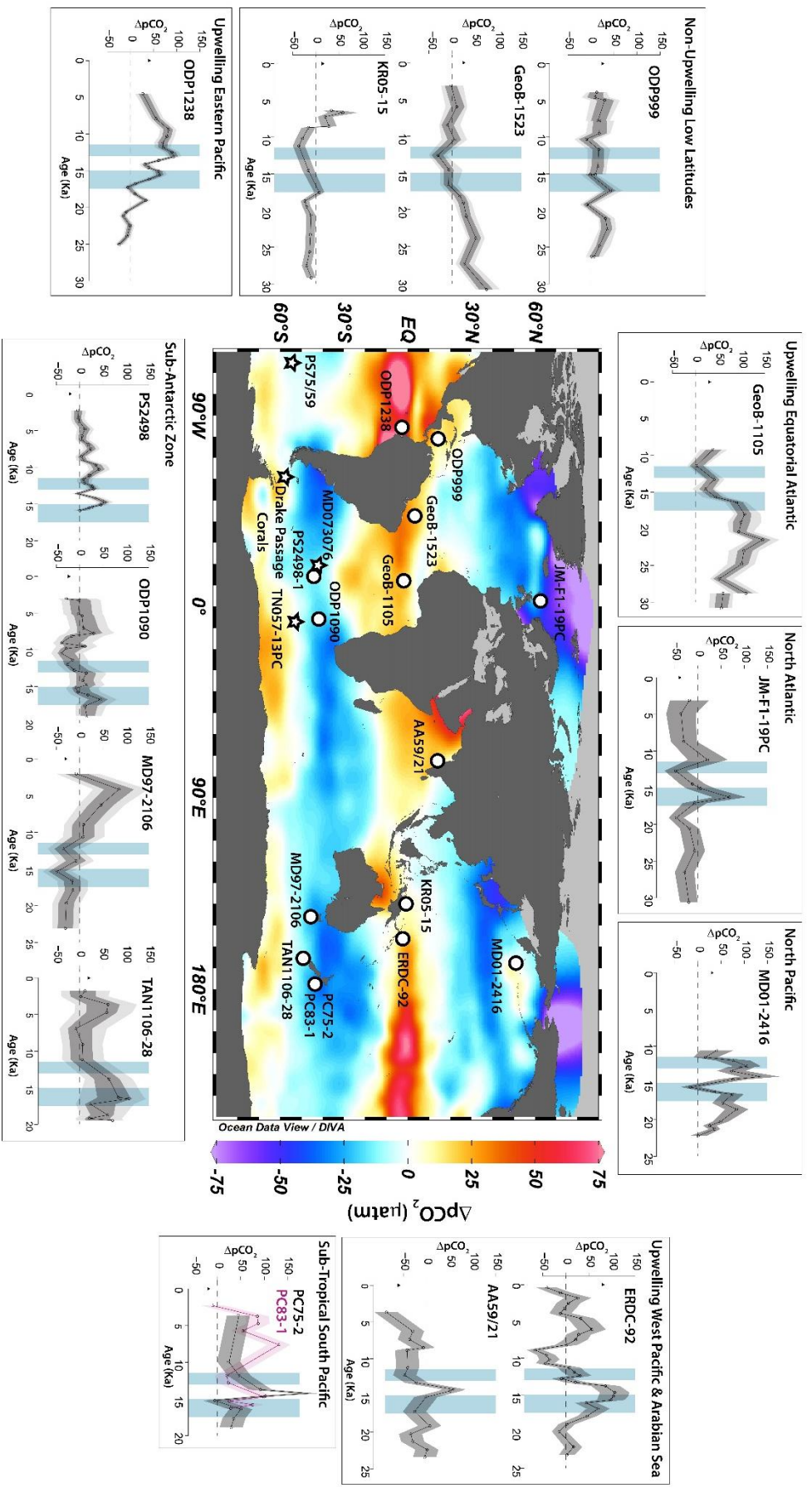
536   **Figure 5. Map of sea surface ΔpCO_2 in the global modern ocean.** Warm (red) colours show areas
537   where the modern ocean is a source of CO_2 to the atmosphere, cold (blue) colours show sink
538   regions. Made in Ocean Data View (https://odv.awi.de/) using the gridded LDEO pCO_2 data of
539   Takahashi et al. (2009) available from (https://odv.awi.de/data/ocean/ldeo-carbon-data/). Datasets
540   taken from Ezat et al. (2017): JM-F1-19PC, Naik et al. (2015): AA59/21, Kubota et al. (2019): KR05-15,
541   Gray et al. (2018): MD01-2416, Palmer and Pearson (2003): ERDC-92, Shao et al. (2019): PC75-2 &
542   PC83-1, this study: TAN1106-28 & ODP1090, Moy et al. (2019): MD97-2106, Martinez-Boti et al.
543   (2015): PS2498 & ODP1238, Foster and Sexton (2014): GeoB-1105, GeoB-1523 & ODP999. In these
544   surrounding plots the two millennial-scale episodes of atmospheric CO_2 rise (Heinrich Stadial 1 (HS1,
545   17.5-15 kyr) and Younger Dryas (YD, 12.9-11.5 kyr)) are highlighted in blue, black triangles show
546   modern ΔpCO_2 values, errors reflect published values, unless otherwise stated in the manuscript.
547   Core locations depicted as stars are the sites referenced in Fig. 1.

548

549
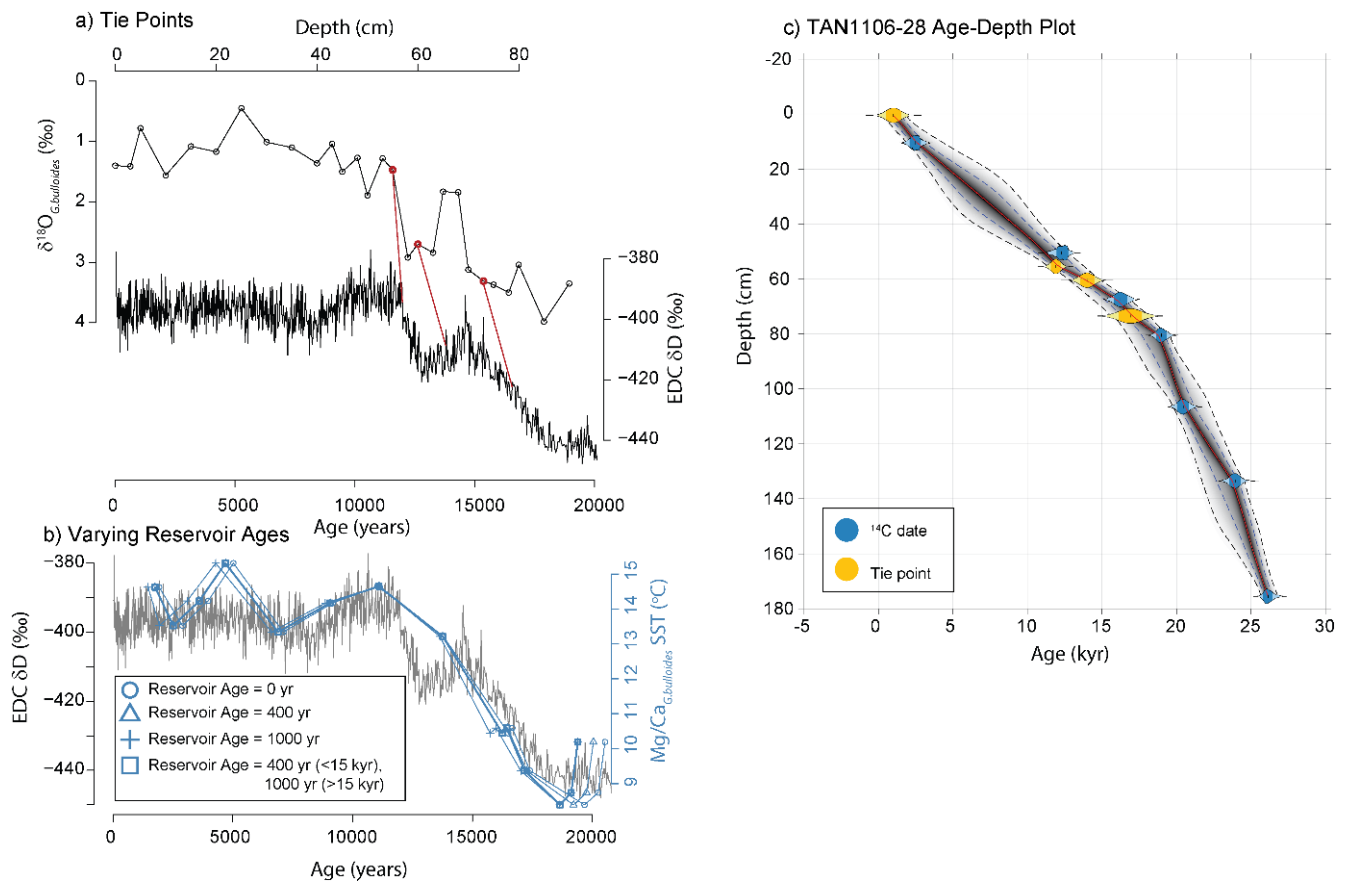
Supplementary Figure 1. Age model for TAN1106-28. a) Shows the $\delta^{18}O_{G.\,bulloides}$ tie points to the AICC2012 δD record. b) Comparison of Mg/Ca$_{G.bulloides}$ derived sea surface temperature (blue) to EPICA Dome C δD Antarctic air temperature record on the AICC2012 age model (grey) (Veres et al., 2013). The variability associated with different reservoir ages is demonstrated by varying shade of blue and symbol (see key). The selected reservoir age is depicted by the bold line with square symbols. c) Age-Depth plot of the age model and the associated age uncertainty.

556

557

558
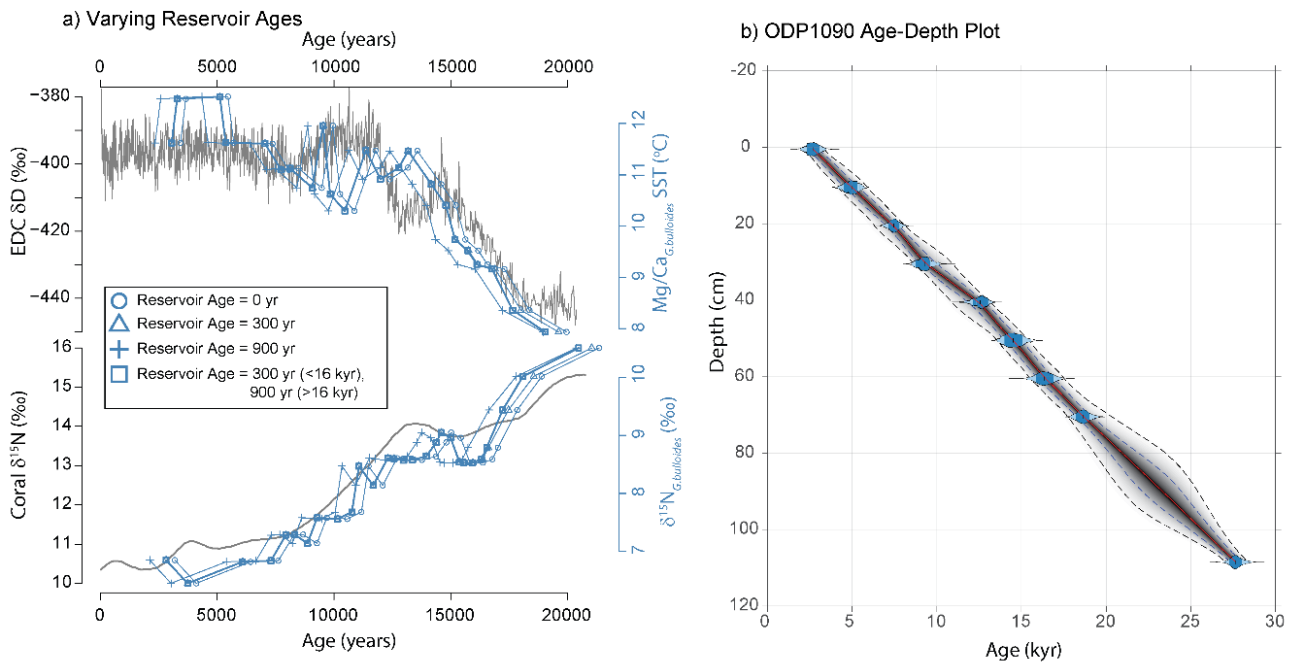
Supplementary Figure 2. Age model for ODP1090. a) Comparison of Mg/Ca_{G.bulloides} derived sea surface temperature (blue) to EPICA Dome C δD Antarctic air temperature record on the AICC2012 age model (grey) (Veres et al., 2013) and of δ^{15}N_{G. bulloides} (blue) to nearby coral δ^{15}N record of Wang et al. (2017) (grey). The variability associated with different reservoir ages is demonstrated by varying shade of blue and symbol (see key). The selected reservoir age is depicted by the bold line with square symbols. c) Age-Depth plot of the age model and the associated age uncertainty.

565

566

567
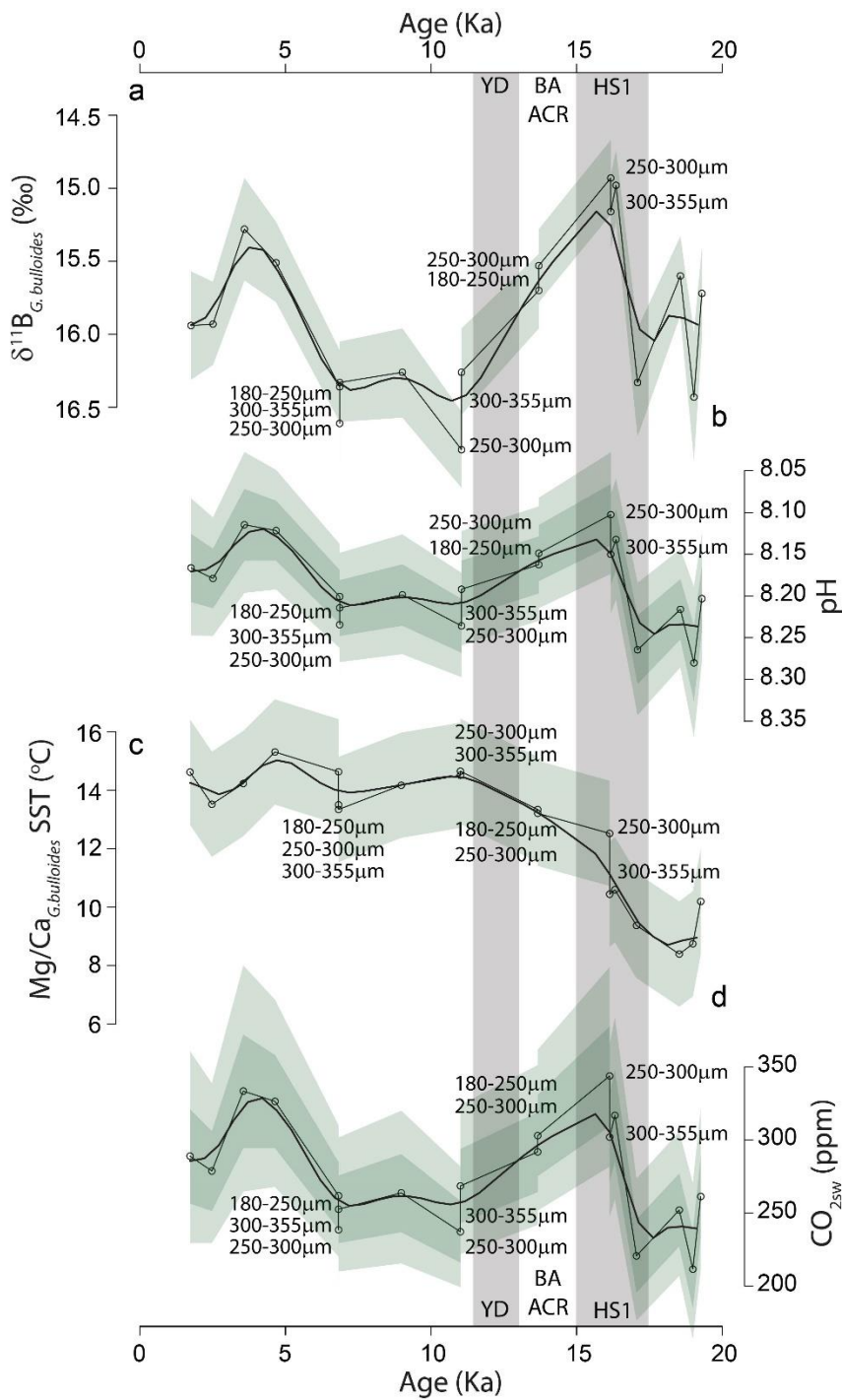
Supplementary Figure 3. Size fraction variability in the δ^{11}B, pH, SST and CO$_{2sw}$ records at site TAN1106-28. Two episodes of major atmospheric CO$_2$ rise (Heinrich Stadial 1 (HS1, 17.5-15 kyr) and Younger Dryas (YD, 12.9-11.5 kyr) are highlighted in grey. **a)** δ^{11}B$_{G.bulloides}$ (‰) with analytical uncertainties (2σ, green envelope). **b)** δ^{11}B$_{G.bulloides}$ derived pH reconstruction with shaded 68% and 95% uncertainty bands. **c)** Mg/Ca$_{G.bulloides}$ based sea surface temperature (SST) record with uncertainty margin used within the uncertainty propagation to calculate CO$_{2sw}$. **d)** δ^{11}B$_{G.bulloides}$ derived CO$_{2sw}$ with shaded 68% and 95% uncertainty bands.

575

7. **References**

ANDERSON, R. F., ALI, S., BRADTMILLER, L. I., NIELSEN, S. H. H., FLEISHER, M. Q., ANDERSON, B. E. & BURCKLE, L. H. 2009. Wind-Driven Upwelling in the Southern Ocean and the Deglacial Rise in Atmospheric CO2. *Science,* 323**,** 1443-1448 doi:10.1126/science.1167441.

ANDERSON, R. F., BARKER, S., FLEISHER, M., GERSONDE, R., GOLDSTEIN, S. L., KUHN, G., MORTYN, P. G., PAHNKE, K. & SACHS, J. P. 2014. Biological response to millennial variability of dust and nutrient supply in the Subantarctic South Atlantic Ocean. *Philosophical Transactions of the Royal Society A: Mathematical, Physical and Engineering Sciences,* 372**,** 20130054 doi:doi:10.1098/rsta.2013.0054.

BAUSKA, T. K., BAGGENSTOS, D., BROOK, E. J., MIX, A. C., MARCOTT, S. A., PETRENKO, V. V., SCHAEFER, H., SEVERINGHAUS, J. P. & LEE, J. E. 2016. Carbon isotopes characterize rapid changes in atmospheric carbon dioxide during the last deglaciation. *Proceedings of the National Academy of Sciences,* 113**,** 3465-3470 doi:10.1073/pnas.1513868113.

BEREITER, B., EGGLESTON, S., SCHMITT, J., NEHRBASS-AHLES, C., STOCKER, T. F., FISCHER, H., KIPFSTUHL, S. & CHAPPELLAZ, J. 2015. Revision of the EPICA Dome C CO2 record from 800 to 600 kyr before present. *Geophysical Research Letters,* 42**,** 542-549 doi:10.1002/2014GL061957.

BOSTOCK, H. C., HAYWARD, B. W., NEIL, H. L., CURRIE, K. I. & DUNBAR, G. B. 2011. Deep-water carbonate concentrations in the southwest Pacific. *Deep Sea Research Part I: Oceanographic Research Papers,* 58**,** 72-85 doi:https://doi.org/10.1016/j.dsr.2010.11.010.

BOSTOCK, H. C., HAYWARD, B. W., NEIL, H. L., SABAA, A. T. & SCOTT, G. H. 2015. Changes in the position of the Subtropical Front south of New Zealand since the last glacial period. *Paleoceanography,* 30**,** 824-844 doi:10.1002/2014PA002652.

BRADTMILLER, L. I., ANDERSON, R. F., FLEISHER, M. Q. & BURCKLE, L. H. 2009. Comparing glacial and Holocene opal fluxes in the Pacific sector of the Southern Ocean. *Paleoceanography,* 24.

BURKE, A. & ROBINSON, L. F. 2012. The Southern Ocean's Role in Carbon Exchange During the Last Deglaciation. *Science,* 335**,** 557-561 doi:10.1126/science.1208163.

CALVO, E., PELEJERO, C. & LOGAN, G. A. 2003. Pressurized liquid extraction of selected molecular biomarkers in deep sea sediments used as proxies in paleoceanography. *Journal of Chromatography A,* 989**,** 197-205 doi:10.1016/S0021-9673(03)00119-5.

CHASE, Z., ANDERSON, R. F., FLEISHER, M. Q. & KUBIK, P. W. 2003. Accumulation of biogenic and lithogenic material in the Pacific sector of the Southern Ocean during the past 40,000 years. *Deep Sea Research Part II: Topical Studies in Oceanography,* 50**,** 799-832 doi:10.1016/S0967-0645(02)00595-7.

COSTA, K. M., HAYES, C. T., ANDERSON, R. F., PAVIA, F. J., BAUSCH, A., DENG, F., DUTAY, J.-C., GEIBERT, W., HEINZE, C., HENDERSON, G., HILLAIRE-MARCEL, C., HOFFMANN, S., JACCARD, S. L., JACOBEL, A. W., KIENAST, S. S., KIPP, L., LERNER, P., LIPPOLD, J., LUND, D., MARCANTONIO, F., MCGEE, D., MCMANUS, J. F., MEKIK, F., MIDDLETON, J. L., MISSIAEN, L., NOT, C., PICHAT, S., ROBINSON, L. F., ROWLAND, G. H., ROY-BARMAN, M., TAGLIABUE, A., TORFSTEIN, A., WINCKLER, G. & ZHOU, Y. 2020. 230Th Normalization: New Insights on an Essential Tool for Quantifying Sedimentary Fluxes in the Modern and Quaternary Ocean. *Paleoceanography and Paleoclimatology,* 35**,** e2019PA003820 doi:10.1029/2019pa003820.

DEVRIES, T. 2014. The oceanic anthropogenic CO2 sink: Storage, air-sea fluxes, and transports over the industrial era. *Global Biogeochemical Cycles,* 28**,** 631-647 doi:10.1002/2013gb004739.

ELDERFIELD, H. & GANSSEN, G. 2000. Past temperature and δ18O of surface ocean waters inferred from foraminiferal Mg/Ca ratios. *Nature,* 405**,** 442 doi:10.1038/35013033.

EZAT, M. M., RASMUSSEN, T. L., HONISCH, B., GROENEVELD, J. & DEMENOCAL, P. 2017. Episodic release of CO2 from the high-latitude North Atlantic Ocean during the last 135 kyr. *Nature Communications,* 8**,** 1-10 doi:10.1038/ncomms14498.

625 FOSTER, G. L. 2008. Seawater pH, PCO2 and CO32- variations in the Caribbean Sea over the last 130
626   kyr: A boron isotope and B/Ca study of planktic forminifera. *Earth and Planetary Science*
627   *Letters,* 271**,** 254-266 doi:10.1016/j.epsl.2008.04.015.
628 FOSTER, G. L., HÖNISCH, B., PARIS, G., DWYER, G. S., RAE, J. W. B., ELLIOTT, T., GAILLARDET, J.,
629   HEMMING, N. G., LOUVAT, P. & VENGOSH, A. 2013. Interlaboratory comparison of boron
630   isotope analyses of boric acid, seawater and marine CaCO3 by MC-ICPMS and NTIMS.
631   *Chemical Geology,* 358**,** 1-14 doi:10.1016/j.chemgeo.2013.08.027.
632 FOSTER, G. L. & RAE, J. W. B. 2016. Reconstructing Ocean pH with Boron Isotopes in Foraminifera.
633   *Annual Review of Earth and Planetary Sciences,* 44**,** 207-237 doi:10.1146/annurev-earth-
634   060115-012226.
635 FOSTER, G. L. & SEXTON, P. F. 2014. Enhanced carbon dioxide outgassing from the eastern equatorial
636   Atlantic during the last glacial. *Geology,* 42**,** 1003-1006 doi:10.1130/G35806.1.
637 FRANCOIS, R., FRANK, M., LOEFF, M. M. R. V. D. & BACON, M. P. 2004. 230Th normalization: An
638   essential tool for interpreting sedimentary fluxes during the late Quaternary.
639   *Paleoceanography,* 19 doi:10.1029/2003PA000939.
640 GALBRAITH, E. D. & JACCARD, S. L. 2015. Deglacial weakening of the oceanic soft tissue pump: global
641   constraints from sedimentary nitrogen isotopes and oxygenation proxies. *Quaternary*
642   *Science Reviews,* 109**,** 38-48 doi:10.1016/j.quascirev.2014.11.012.
643 GALBRAITH, E. D., JACCARD, S. L., PEDERSEN, T. F., SIGMAN, D. M., HAUG, G. H., COOK, M.,
644   SOUTHON, J. R. & FRANCOIS, R. 2007. Carbon dioxide release from the North Pacific abyss
645   during the last deglaciation. *Nature,* 449**,** 890-893
646   doi:http://www.nature.com/nature/journal/v449/n7164/suppinfo/nature06227_S1.html.
647 GALBRAITH, E. D. & SKINNER, L. C. 2020. The Biological Pump During the Last Glacial Maximum.
648   *Annual Review of Marine Science,* 12**,** 559-586 doi:10.1146/annurev-marine-010419-
649   010906.
650 GOTTSCHALK, J., SKINNER, L. C., LIPPOLD, J., VOGEL, H., FRANK, N., JACCARD, S. L. & WAELBROECK,
651   C. 2016. Biological and physical controls in the Southern Ocean on past millennial-scale
652   atmospheric CO2 changes. *Nature Communications,* 7**,** 11539 doi:10.1038/ncomms11539.
653 GRAY, W. R., RAE, J. W. B., WILLS, R. C. J., SHEVENELL, A. E., TAYLOR, B., BURKE, A., FOSTER, G. L. &
654   LEAR, C. H. 2018. Deglacial upwelling, productivity and CO2 outgassing in the North Pacific
655   Ocean. *Nature Geoscience,* 11**,** 340-344 doi:10.1038/s41561-018-0108-6.
656 HAIN, M. P., FOSTER, G. L. & CHALK, T. 2018. Robust Constraints on Past CO2 Climate Forcing From
657   the Boron Isotope Proxy. *Paleoceanography and Paleoclimatology,* 33**,** 1099-1115
658   doi:10.1029/2018pa003362.
659 HENEHAN, M. J., FOSTER, G. L., BOSTOCK, H. C., GREENOP, R., MARSHALL, B. J. & WILSON, P. A.
660   2016. A new boron isotope-pH calibration for Orbulina universa, with implications for
661   understanding and accounting for 'vital effects'. *Earth and Planetary Science Letters,* 454**,**
662   282-292 doi:10.1016/j.epsl.2016.09.024.
663 HENEHAN, M. J., FOSTER, G. L., RAE, J. W. B., PRENTICE, K. C., EREZ, J., BOSTOCK, H. C., MARSHALL, B.
664   J. & WILSON, P. A. 2015. Evaluating the utility of B/Ca ratios in planktic foraminifera as a
665   proxy for the carbonate system: A case study of Globigerinoides ruber. *Geochemistry,*
666   *Geophysics, Geosystems,* 16**,** 1052-1069 doi:10.1002/2014gc005514.
667 HOGG, A. G., HUA, Q., BLACKWELL, P. G., NIU, M., BUCK, C. E., GUILDERSON, T. P., HEATON, T. J.,
668   PALMER, J. G., REIMER, P. J., REIMER, R. W., TURNEY, C. S. M. & ZIMMERMAN, S. R. H. 2016.
669   SHCal13 Southern Hemisphere Calibration, 0–50,000 Years cal BP. *Radiocarbon,* 55**,** 1889-
670   1903 doi:10.2458/azu_js_rc.55.16783.
671 JACCARD, S., HAYES, C. T., MARTÍNEZ-GARCÍA, A., HODELL, D., ANDERSON, R. F., SIGMAN, D. M. &
672   HAUG, G. 2013. Two modes of change in Southern Ocean productivity over the past million
673   years. *Science,* 339**,** 1419-1423 doi:10.1126/science.1227545.

674   JACCARD, S. L. & GALBRAITH, E. D. 2012. Large climate-driven changes of oceanic oxygen
675   concentrations during the last deglaciation. *Nature Geoscience,* 5**,** 151-156
676   doi:10.1038/ngeo1352.
677   JACCARD, S. L., GALBRAITH, E. D., MARTÍNEZ-GARCÍA, A. & ANDERSON, R. F. 2016. Covariation of
678   deep Southern Ocean oxygenation and atmospheric CO2 through the last ice age. *Nature,*
679   530**,** 207-210 doi:10.1038/nature16514.
680   KISS, E. 1988. Ion-exchange separation and spectrophotometric determination of boron in geological
681   materials. *Analytica Chimica Acta,* 211**,** 243-256 doi:10.1016/S0003-2670(00)83684-3.
682   KÖHLER, P., JOOS, F., GERBER, S. & KNUTTI, R. 2005. Simulated changes in vegetation distribution,
683   land carbon storage, and atmospheric CO2 in response to a collapse of the North Atlantic
684   thermohaline circulation. *Climate Dynamics,* 25**,** 689 doi:10.1007/s00382-005-0058-8.
685   KORNILOVA, O. & ROSELL-MELÉ, A. 2003. Application of microwave-assisted extraction to the
686   analysis of biomarker climate proxies in marine sediments. *Organic Geochemistry,* 34**,** 1517-
687   1523 doi:10.1016/S0146-6380(03)00155-4.
688   KUBOTA, K., YOKOYAMA, Y., ISHIKAWA, T., SAGAWA, T., IKEHARA, M. & YAMAZAKI, T. 2019.
689   Equatorial Pacific seawater pCO2 variability since the last glacial period. *Scientific Reports,* 9**,**
690   13814 doi:10.1038/s41598-019-49739-0.
691   LAMBERT, F., BIGLER, M., STEFFENSEN, J. P., HUTTERLI, M. & FISCHER, H. 2012. Centennial mineral
692   dust variability in high-resolution ice core data from Dome C, Antarctica. *Clim. Past,* 8**,** 609-
693   623 doi:10.5194/cp-8-609-2012.
694   LAMY, F., GERSONDE, R., WINCKLER, G., ESPER, O., JAESCHKE, A., KUHN, G., ULLERMANN, J.,
695   MARTÍNEZ-GARCIA, A., LAMBERT, F. & KILIAN, R. 2014. Increased dust deposition in the
696   Pacific Southern Ocean during glacial periods. *Science,* 343**,** 403-407
697   doi:10.1126/science.1245424.
698   LEMARCHAND, D., GAILLARDET, J., GÖPEL, C. & MANHÈS, G. 2002. An optimized procedure for boron
699   separation and mass spectrometry analysis for river samples. *Chemical Geology,* 182**,** 323-
700   334 doi:10.1016/S0009-2541(01)00329-1.
701   LOUGHEED, B. C. & OBROCHTA, S. P. 2019. A Rapid, Deterministic Age-Depth Modeling Routine for
702   Geological Sequences With Inherent Depth Uncertainty. *Paleoceanography and*
703   *Paleoclimatology,* 34**,** 122-133 doi:10.1029/2018pa003457.
704   MARTINEZ-BOTI, M. A., MARINO, G., FOSTER, G. L., ZIVERI, P., HENEHAN, M. J., RAE, J. W. B.,
705   MORTYN, P. G. & VANCE, D. 2015. Boron isotope evidence for oceanic carbon dioxide
706   leakage during the last deglaciation. *Nature,* 518**,** 219-222 doi:10.1038/nature14155.
707   MARTÍNEZ-BOTÍ, M. A., MARINO, G., FOSTER, G. L., ZIVERI, P., HENEHAN, M. J., RAE, J. W. B.,
708   MORTYN, P. G. & VANCE, D. 2015. Boron isotope evidence for oceanic carbon dioxide
709   leakage during the last deglaciation. *Nature,* 518**,** 219-222 doi:10.1038/nature14155.
710   MARTÍNEZ-GARCÍA, A., SIGMAN, D. M., REN, H., ANDERSON, R. F., STRAUB, M., HODELL, D. A.,
711   JACCARD, S. L., EGLINTON, T. I. & HAUG, G. H. 2014. Iron Fertilization of the Subantarctic
712   Ocean During the Last Ice Age. *Science,* 343**,** 1347-1350 doi:10.1126/science.1246848.
713   MAXSON, C. R., BOSTOCK, H. C., MACKINTOSH, A., MIKALOFF-FLETCHER, S., MCCAVE, N. & NEIL, H. L.
714   2019. Modern, Preindustrial, and Past (Last 25 ka) Carbon Isotopic (δ13C) Variability in the
715   Surface Waters of the Southwest Pacific. *Paleoceanography and Paleoclimatology,* 34**,** 692-
716   714 doi:10.1029/2018PA003441.
717   MOY, A. D., PALMER, M. R., HOWARD, W. R., BIJMA, J., COOPER, M. J., CALVO, E., PELEJERO, C.,
718   GAGAN, M. K. & CHALK, T. B. 2019. Varied contribution of the Southern Ocean to deglacial
719   atmospheric CO2 rise. *Nature Geoscience,* 12**,** 1006-1011 doi:10.1038/s41561-019-0473-9.
720   NAIK, S. S., DIVAKAR NAIDU, P., FOSTER, G. L. & MARTÍNEZ-BOTÍ, M. A. 2015. Tracing the strength of
721   the southwest monsoon using boron isotopes in the eastern Arabian Sea. *Geophysical*
722   *Research Letters,* 42**,** 1450-1458 doi:10.1002/2015GL063089.

723   NINNEMANN, U. S. & CHARLES, C. D. 1997. Regional differences in Quaternary subantarctic nutrient
724   cycling: Link to intermediate and deep water ventilation. *Paleoceanography,* 12**,** 560-567
725   doi:10.1029/97pa01032.
726   PALMER, M. R. & PEARSON, P. N. 2003. A 23,000-Year Record of Surface Water pH and pCO2 in the
727   Western Equatorial Pacific Ocean. *Science,* 300**,** 480-482 doi:10.1126/science.1080796.
728   RAE, J. W. B., BURKE, A., ROBINSON, L. F., ADKINS, J. F., CHEN, T., COLE, C., GREENOP, R., LI, T.,
729   LITTLEY, E. F. M., NITA, D. C., STEWART, J. A. & TAYLOR, B. J. 2018. CO2 storage and release
730   in the deep Southern Ocean on millennial to centennial timescales. *Nature,* 562**,** 569-573
731   doi:10.1038/s41586-018-0614-0.
732   RAE, J. W. B., FOSTER, G. L., SCHMIDT, D. N. & ELLIOTT, T. 2011. Boron isotopes and B/Ca in benthic
733   foraminifera: Proxies for the deep ocean carbonate system. *Earth and Planetary Science*
734   *Letters,* 302**,** 403-413 doi:10.1016/j.epsl.2010.12.034.
735   RAITZSCH, M., BIJMA, J., BENTHIEN, A., RICHTER, K.-U., STEINHOEFEL, G. & KUČERA, M. 2018. Boron
736   isotope-based seasonal paleo-pH reconstruction for the Southeast Atlantic – A multispecies
737   approach using habitat preference of planktonic foraminifera. *Earth and Planetary Science*
738   *Letters,* 487**,** 138-150 doi:10.1016/j.epsl.2018.02.002.
739   ROBERTS, J., GOTTSCHALK, J., SKINNER, L. C., PECK, V. L., KENDER, S., ELDERFIELD, H., WAELBROECK,
740   C., VÁZQUEZ RIVEIROS, N. & HODELL, D. A. 2016. Evolution of South Atlantic density and
741   chemical stratification across the last deglaciation. *Proceedings of the National Academy of*
742   *Sciences,* 113**,** 514-519 doi:10.1073/pnas.1511252113.
743   SARMIENTO, J. L., GRUBER, N., BRZEZINSKI, M. A. & DUNNE, J. P. 2004. High-latitude controls of
744   thermocline nutrients and low latitude biological productivity. *Nature,* 427**,** 56
745   doi:10.1038/nature02127.
746   SCHMITT, J., SCHNEIDER, R., ELSIG, J., LEUENBERGER, D., LOURANTOU, A., CHAPPELLAZ, J., KÖHLER,
747   P., JOOS, F., STOCKER, T. F., LEUENBERGER, M. & FISCHER, H. 2012. Carbon Isotope
748   Constraints on the Deglacial CO2 Rise from Ice Cores. *Science,* 336**,** 711-714
749   doi:10.1126/science.1217161.
750   SHAO, J., STOTT, L. D., GRAY, W. R., GREENOP, R., PECHER, I., NEIL, H. L., COFFIN, R. B., DAVY, B. &
751   RAE, J. W. B. 2019. Atmosphere-Ocean CO2 Exchange Across the Last Deglaciation from the
752   Boron Isotope Proxy. *Paleoceanography and Paleoclimatology,* 34**,** 1650-1670
753   doi:10.1029/2018pa003498.
754   SIGMAN, D. M., HAIN, M. P. & HAUG, G. H. 2010. The polar ocean and glacial cycles in atmospheric
755   CO2 concentration. *Nature,* 466**,** 47-55 doi:10.1038/nature09149.
756   SKINNER, L., MCCAVE, I. N., CARTER, L., FALLON, S., SCRIVNER, A. E. & PRIMEAU, F. 2015. Reduced
757   ventilation and enhanced magnitude of the deep Pacific carbon pool during the last glacial
758   period. *Earth and Planetary Science Letters,* 411**,** 45-52
759   doi:https://doi.org/10.1016/j.epsl.2014.11.024.
760   SKINNER, L. C., FALLON, S., WAELBROECK, C., MICHEL, E. & BARKER, S. 2010. Ventilation of the Deep
761   Southern Ocean and Deglacial CO2 Rise. *Science,* 328**,** 1147-1151
762   doi:10.1126/science.1183627.
763   SKINNER, L. C., WAELBROECK, C., SCRIVNER, A. E. & FALLON, S. J. 2014. Radiocarbon evidence for
764   alternating northern and southern sources of ventilation of the deep Atlantic carbon pool
765   during the last deglaciation. *Proceedings of the National Academy of Sciences,* 111**,** 5480-
766   5484 doi:10.1073/pnas.1400668111.
767   SPERO, H. J. & LEA, D. W. 2002. The Cause of Carbon Isotope Minimum Events on Glacial
768   Terminations. *Science,* 296**,** 522-525 doi:10.1126/science.1069401.
769   STEWART, J. A., CHRISTOPHER, S. J., KUCKLICK, J. R., BORDIER, L., CHALK, T. B., DAPOIGNY, A.,
770   DOUVILLE, E., FOSTER, G. L., GRAY, W. R., GREENOP, R., GUTJAHR, M., HEMSING, F.,
771   HENEHAN, M. J., HOLDSHIP, P., HSIEH, Y.-T., KOLEVICA, A., LIN, Y.-P., MAWBEY, E. M., RAE, J.
772   W. B., ROBINSON, L. F., SHUTTLEWORTH, R., YOU, C.-F., ZHANG, S. & DAY, R. D. NIST RM
773   8301 Boron Isotopes in Marine Carbonate (Simulated Coral and Foraminifera Solutions):

774   Inter-laboratory δ11B and Trace Element Ratio Value Assignment. *Geostandards and*
775   *Geoanalytical Research,* n/a doi:10.1111/ggr.12363.
776 STUDER, A. S., SIGMAN, D. M., MARTÍNEZ-GARCÍA, A., BENZ, V., WINCKLER, G., KUHN, G., ESPER, O.,
777   LAMY, F., JACCARD, S. L., WACKER, L., OLEYNIK, S., GERSONDE, R. & HAUG, G. H. 2015.
778   Antarctic Zone nutrient conditions during the last two glacial cycles. *Paleoceanography,* 30**,**
779   845-862 doi:10.1002/2014pa002745.
780 TAKAHASHI, T., SUTHERLAND, S. C., WANNINKHOF, R., SWEENEY, C., FEELY, R. A., CHIPMAN, D. W.,
781   HALES, B., FRIEDERICH, G., CHAVEZ, F., SABINE, C., WATSON, A., BAKKER, D. C. E., SCHUSTER,
782   U., METZL, N., YOSHIKAWA-INOUE, H., ISHII, M., MIDORIKAWA, T., NOJIRI, Y., KÖRTZINGER,
783   A., STEINHOFF, T., HOPPEMA, M., OLAFSSON, J., ARNARSON, T. S., TILBROOK, B.,
784   JOHANNESSEN, T., OLSEN, A., BELLERBY, R., WONG, C. S., DELILLE, B., BATES, N. R. & DE
785   BAAR, H. J. W. 2009. Climatological mean and decadal change in surface ocean pCO2, and
786   net sea–air CO2 flux over the global oceans. *Deep Sea Research Part II: Topical Studies in*
787   *Oceanography,* 56**,** 554-577 doi:10.1016/j.dsr2.2008.12.009.
788 TAKAHASHI, T., SWEENEY, C., HALES, B., CHIPMAN, D., NEWBERGER, T., GODDARD, J., IANNUZZI, R.
789   & SUTHERLAND, S. 2012. The Changing Carbon Cycle in the Southern Ocean. *Oceanography,*
790   25**,** 26-37 doi:10.5670/oceanog.2012.71.
791 THÖLE, L. M., AMSLER, H. E., MORETTI, S., AUDERSET, A., GILGANNON, J., LIPPOLD, J., VOGEL, H.,
792   CROSTA, X., MAZAUD, A., MICHEL, E., MARTÍNEZ-GARCÍA, A. & JACCARD, S. L. 2019. Glacial-
793   interglacial dust and export production records from the Southern Indian Ocean. *Earth and*
794   *Planetary Science Letters,* 525**,** 115716 doi:10.1016/j.epsl.2019.115716.
795 TOGGWEILER, J. R. 1999. Variation of atmospheric CO2 by ventilation of the ocean's deepest water.
796   *Paleoceanography,* 14**,** 571-588 doi:10.1029/1999PA900033.
797 TOGGWEILER, J. R., DRUFFEL, E. R. M., KEY, R. M. & GALBRAITH, E. D. 2019. Upwelling in the Ocean
798   Basins North of the ACC: 2. How Cool Subantarctic Water Reaches the Surface in the Tropics.
799   *Journal of Geophysical Research: Oceans,* 124**,** 2609-2625 doi:10.1029/2018jc014795.
800 TRUDGILL, M., SHUTTLEWORTH, R., BOSTOCK, H. C., BURKE, A., COOPER, M. J., GREENOP, R. &
801   FOSTER, G. L. Submitted. The Flux and Provenance of Dust Delivered to the SW Pacific During
802   the Last Glacial Maximum. *Paleoceanography and Paleoclimatology*.
803 VENZ, K. A. & HODELL, D. A. 2002. New evidence for changes in Plio–Pleistocene deep water
804   circulation from Southern Ocean ODP Leg 177 Site 1090. *Palaeogeography,*
805   *Palaeoclimatology, Palaeoecology,* 182**,** 197-220 doi:10.1016/S0031-0182(01)00496-5.
806 VERES, D., BAZIN, L., LANDAIS, A., TOYÉ MAHAMADOU KELE, H., LEMIEUX-DUDON, B., PARRENIN, F.,
807   MARTINERIE, P., BLAYO, E., BLUNIER, T., CAPRON, E., CHAPPELLAZ, J., RASMUSSEN, S. O.,
808   SEVERI, M., SVENSSON, A., VINTHER, B. & WOLFF, E. W. 2013. The Antarctic ice core
809   chronology (AICC2012): an optimized multi-parameter and multi-site dating approach for
810   the last 120 thousand years. *Clim. Past,* 9**,** 1733-1748 doi:10.5194/cp-9-1733-2013.
811 VILLANUEVA, J., PELEJERO, C. & GRIMALT, J. O. 1997. Clean-up procedures for the unbiased
812   estimation of C37 alkenone sea surface temperatures and terrigenous n-alkane inputs in
813   paleoceanography. *Journal of Chromatography A,* 757**,** 145-151 doi:10.1016/S0021-
814   9673(96)00669-3.
815 WANG, X. T., SIGMAN, D. M., PROKOPENKO, M. G., ADKINS, J. F., ROBINSON, L. F., HINES, S. K., CHAI,
816   J., STUDER, A. S., MARTÍNEZ-GARCÍA, A., CHEN, T. & HAUG, G. H. 2017. Deep-sea coral
817   evidence for lower Southern Ocean surface nitrate concentrations during the last ice age.
818   *Proceedings of the National Academy of Sciences,* 114**,** 3352-3357
819   doi:10.1073/pnas.1615718114.
820 ZIEGLER, M., DIZ, P., HALL, I. R. & ZAHN, R. 2013. Millennial-scale changes in atmospheric CO2 levels
821   linked to the Southern Ocean carbon isotope gradient and dust flux. *Nature Geoscience,* 6**,**
822   457-461 doi:10.1038/ngeo1782.

823